Astronomy & Astrophysics manuscript no. paperrI˙FINAL
April 2, 2014
© ESO 2014

arXiv:1404.0234v1 [astro-ph.SR] 1 Apr 2014

High-resolution abundance analysis of very metal-poor r-I stars ⋆

C. Siqueira Mello[1], V. Hill[2], B. Barbuy[1], M. Spite[3], F. Spite[3], T.C. Beers[4], E. Caffau[3], P. Bonifacio[3], R. Cayrel[3], P. François[5], H. Schatz[6], and S. Wanajo[7,8]

[1] IAG, Universidade de São Paulo, Rua do Matão 1226, Cidade Universitária, São Paulo 05508-900, Brazil
[2] Université de Sophia-Antipolis, Observatoire de la Côte d'Azur, CNRS UMR 6202, BP4229, 06304 Nice Cedex 4, France
[3] GEPI, Observatoire de Paris, CNRS, UMR 8111, F-92195 Meudon Cedex, France
[4] National Optical Astronomy Observatory, Tucson, Arizona 85719, USA and JINA: Joint Institute for Nuclear Physics; email: beers@noao.edu
[5] GEPI, Observatoire de Paris, CNRS, UMR 8111, 61 Av. de l'Observatoire, 75014 Paris, France
[6] National Superconducting Cyclotron Laboratory, Department of Physics and Astronomy and Joint Institute for Nuclear Astrophysics, Michigan State University, East Lansing, MI 48824, USA; email: schatz@nscl.msu.edu
[7] National Astronomical Observatory of Japan, 2-21-1 Osawa, Mitaka, Tokyo 181-8588, Japan; email: shinya.wanajo@nao.ac.jp
[8] RIKEN, iTHES Research Group, 2-1 Hirosawa, Wako, Saitama, 351-0198, Japan

Received 18 March 2014; accepted 28 March 2014

ABSTRACT

Context. Moderately r-process-enriched stars (r-I; $+0.3 \leq$ [Eu/Fe] $\leq +1.0$) are at least four times as common as those that are greatly enriched in r-process elements (r-II; [Eu/Fe] $> +1.0$), and the abundances in their atmospheres are important tools for obtaining a better understanding of the nucleosynthesis processes responsible for the origin of the elements beyond the iron peak.
Aims. The main aim of this work is to derive abundances for a sample of seven metal-poor stars with $-3.4 \leq$ [Fe/H] ≤ -2.4 classified as r-I stars, to understand the role of these stars for constraining the astrophysical nucleosynthesis event(s) that is(are) responsible for the production of the r-process, and to investigate whether they differ, in any significant way, from the r-II stars.
Methods. We carried out a detailed abundance analysis based on high-resolution spectra obtained with the VLT/UVES spectrograph, using spectra in the wavelength ranges 3400 - 4500 Å, 6800 - 8200 Å, and 8700 - 10,000 Å, with resolving power R $\sim$ 40 000 (blue arm) and R $\sim$ 55 000 (red arm). The OSMARCS LTE 1D model atmosphere grid was employed, along with the spectrum synthesis code Turbospectrum.
Results. We have derived abundances of the light elements Li, C, and N, the α-elements Mg, Si, S, Ca, and Ti, the odd-Z elements Al, K, and Sc, the iron-peak elements V, Cr, Mn, Fe, Co, and Ni, and the trans-iron elements from the first peak (Sr, Y, Zr, Mo, Ru, and Pd), the second peak (Ba, La, Ce, Pr, Nd, Sm, Eu, Gd, Tb, Dy, Ho, Er, Tm, and Yb), the third peak (Os and Ir, as upper limits), and the actinides (Th) regions. The results are compared with values for these elements for r-II and "normal" very and extremely metal-poor stars reported in the literature, ages based on radioactive chronometry are explored using different models, and a number of conclusions about the r-process and the r-I stars are presented. Hydrodynamical models were used for some elements, and general behaviors for the 3D corrections were presented. Although the abundance ratios of the second r-process peak elements (usually associated with the main r-process) are nearly identical for r-I and r-II stars, the first r-process peak abundance ratios (probably associated with the weak r-process) are more enhanced in r-I stars than in r-II stars, suggesting that differing nucleosynthesis pathways were followed by stars belonging to these two different classifications.

Key words. Galaxy: Halo - Stars: Abundances - Nucleosynthesis

1. Introduction

The heavy elements (those beyond the iron-peak elements) are primarily formed by the capture of neutrons. This process takes place through the slow (s) or the rapid (r) process, where the addition of a neutron is considered slow or rapid relative to the time for β decay to take place (which differs from isotope to isotope). The main s-process is thought to occur on a relatively long timescale in asymptotic giant branch (AGB) stars (see, e.g., Herwig 2005, Sneden et al. 2008). The r-process instead occurs on a rather short timescale, typical of supernovae explosions (e.g., Winteler et al. 2012; Wanajo 2013) or other brief events, such as neutron star mergers (e.g., Goriely et al. 2011; Korobkin et al. 2012; Rosswog et al. 2014; Wanajo et al. 2014). In the early evolution of the Galaxy, matter may have been enriched in heavy elements through the r-process alone, as first suggested by Truran (1981) (see also Roederer et al. 2010, 2014, and references therein). To date, full understanding of r-process nucleosynthesis and the astrophysical sites that account for its operation remain unclear (e.g., Wanajo & Ishimaru 2006; Kratz et al. 2007; Langanke & Thielemann 2013). The best sources of information to constrain this process are the abundances of very and extremely metal-poor stars, since they contain the nucleosythesis products from early generations of stars and are essentially unaltered by later production events.

Beers & Christlieb (2005) classified metal-poor stars in terms of their metallicities and the enhancements of carbon and the r- and s-process elements. Metal-poor stars that are enhanced in the neutron-capture elements provide a unique opportunity to study the r-process in the early Galaxy *in situ*, even for extremely metal-poor stars ([Fe/H] < -3.0). In the absence of enhance-

Send offprint requests to: C. Siqueira Mello Jr. (cesar.mello@usp.br).

⋆ Observations obtained with the VLT, at the European Southern Observatory, Paranal, Chile, under proposal 080.D-0194(A) (PI:V. Hill)

ment of the neutron-capture elements, most species would be too weak to be detected in high-resolution spectra. Two classes of metal-poor stars were defined by Beers & Christlieb (2005) according to their enhancement in r-process elements – the moderately r-process-enhanced stars, with $+0.3 \leq$ [Eu/Fe][1] $\leq +1.0$ and [Ba/Eu] < 0, designated as r-I stars, and the highly r-process-enhanced stars, with [Eu/Fe] $> +1.0$ and [Ba/Eu] < 0, designated as r-II stars. According to Beers & Christlieb (2005), the r-I stars appear to be, on the whole, at least several times as common as their more extreme counterparts, the r-II stars.

In the context of the Hamburg/ESO R-process Enhanced Star survey (HERES) (Christlieb et al. 2004; Barklem et al. 2005, hereafter B05), 253 metal-poor halo stars in the metallicity range $-3.8 <$ [Fe/H] < -1.5 were studied. The spectra were obtained with the VLT/UVES spectrograph, using a slit width of 2", yielding a resolving power R $\sim$ 20 000, and a typical signal-to-noise ratio S/N $\sim$ 50 per pixel, covering the wavelength region 3760 - 4980 Å. Based on these observations, B05 identified 8 r-II and 35 r-I stars, showing that the r-I stars are, in fact, more than four times as common as the r-II stars.

Barklem et al. (2005) (and others before) suggested that the pattern of the neutron-capture elements of r-II stars, including the reference stars CS 22892-052 (McWilliam et al. 1995; Sneden et al. 1996, 2000, 2009) and CS 31082-001 (Cayrel et al. 2001; Hill et al. 2002), closely followed the scaled solar system r-process abundances for elements beyond barium (except for Th and U). In stars of lower r-element enrichment, such as the r-I stars, B05 noted that the lighter element abundances (in particular Sr, Y, Zr) are generally higher than expected from the solar pattern. Moreover, r-II stars were found to occupy a narrow metallicity range, centered on [Fe/H] ~ -2.8, with a small scatter ($\sim$ 0.16 dex). The r-I stars, on the other hand, were found to occur across a wide metallicity range. From the data of B05, the abundance ratios from [C/Fe] to [Zn/Fe] appeared to be the same in the r-II, r-I stars, and normal metal-poor stars (those without CNO or neutron-capture enhancements). These results have been strengthened, with only a few exceptions, by high-resolution spectroscopic observations of additional metal-poor stars in recent years.

Based on the analysis of a sample of metal-poor stars with $-3.4 \leq$ [Fe/H] ≤ -2.4 classified as r-I stars, the purpose of the present paper is to perform a detailed comparison of the abundance ratios of elements for the r-I and r-II stars, and thereby gain a better understanding of the nature of the r-process and the likely astrophysical site(s) with which it might be associated. In Sect. 2, the observations and reductions are reported. Sect. 3 describes the abundance determinations. In Sect. 4, the results are provided, followed by a discussion in Sect. 5. Conclusions are given in Sect. 6.

2. Observations and reductions

Seven r-I stars were selected from the list of B05, with [Fe/H] ≤ -2.3, since, at higher metallicity, enrichment of the interstellar medium from which these stars were born with s-process elements contributed by AGB stars becomes more of a problem (see, e.g., François et al. 2007). We also discarded the carbon-enhanced metal-poor (CEMP) stars, since many of these stars have been enriched in C and heavy s-process elements, because of mass-transfer from an AGB companion. The atmospheric parameters of the selected stars (from B05) are given in Table 1, along with their reported [Eu/Fe], [Ba/Eu], and [C/Fe], the abundance ratios upon which their original classification was based.

The seven r-I stars were observed with the VLT/UVES spectrograph in November 6 - 10, 2007. The blue and red arms were centered on 3900 Å and 8600 Å, and the spectra were obtained with a 1" slit, a resolving power of R $\sim$ 40 000 and R $\sim$ 55 000, respectively, with about five pixels per resolution element. Spectra in the wavelength ranges 3400 - 4500 Å, 6800 - 8200 Å, and 8700 - 10,000 Å were obtained. The log of observations is given in Table 2. Standard data reductions were performed, employing the UVES pipeline in the ESO - GASGANO environment, including flatfield correction, bias and dark subtraction, cosmic-ray removal, spectral extraction, and wavelength calibration with comparison arc-line spectra taken before or after each exposure.

In the frame of the Large Program (LP) "First Stars" (PI: R. Cayrel), some 35 very metal-poor giants were analyzed based on very high-quality high-resolution spectra. The abundance patterns from C to Zn are presented in Cayrel et al. (2004), and also (for very metal-poor main-sequence turnoff stars) in Bonifacio et al. (2009). François et al. (2007) derived the abundance patterns of the neutron-capture elements for many of these stars. Among the giants, six r-I stars and three r-II stars (CS 31082-001, CS 22953-003, and CS 22892-052) were studied in detail and were added to the present sample of r-I stars for the purpose of discussion. The relative abundances of the heavy elements for CS 31082-001 come from Hill et al. (2002), Barbuy et al. (2011), and Siqueira-Mello et al. (2013), for CS 22953-003 they were taken from François et al. (2007), and for CS 22892-052 from Sneden et al. (1996, 2000, 2009).

For the star CS 30315-029, we also used a spectrum obtained during the LP "First Stars," in the regions centered on 3960 Å and 5730 Å, to measure the Ba lines. For the other six stars, we derived Ba abundances from the HERES spectra.

2.1. Radial velocities

For each spectrum, Table 2 lists the measured geocentric (RV_G) and barycentric (RV_B) radial velocities, along with the mean RV_B for each star. These measurements were made with the blue spectra; a precision of about 1 km s^{-1}was achieved.

Comparison to the values given by B05 shows good agreement, within the error bars. Consequently, our sample stars do not present any indication of binarity.

2.2. Measurement of equivalent widths

The spectra were normalized, corrected for radial-velocity shifts, and combined to produce the final average data. We measured the equivalent widths (EW) of a set of weak iron and titanium lines in their neutral and ionized states. The EWs were measured with a semi-automatic code, which traces the continuum and uses a Gaussian profile to fit the absorption lines. The central wavelength of each line was left as a free parameter, and the full width at half maximum (FWHM) was computed as well. For blends on the blue or the red wing, this part of the line can be excluded from the computations. The EWs of the Fe and Ti lines used in this work are given in Table A.1 along with the corresponding log gf values.

To check the reliability of the implemented code, the results were compared with those obtained using Fitline (François et al. 2003), an automated line-fitting procedure based on the algorithms of Charbonneau (1995). Fig. 1 shows a comparison of

[1] We adopt the notation [A/B] = $\log(n_A/n_B)_{star}$ - $\log(n_A/n_B)_{\odot}$, where n is the number density of atoms.

Table 1. Atmospheric parameters, radial velocities, [Eu/Fe], [Ba/Eu], and [C/Fe] taken from Barklem et al. (2005). Our set of stars were chosen with $+0.3 \leq$ [Eu/Fe] $\leq +1.0$ and [Ba/Eu] < 0.

Star	$T_{\rm eff}$	log$g$	[Fe/H]	ξ	V_r	[Eu/Fe]	[Ba/Eu]	[C/Fe]
	(K)	[cgs]		(km s^{-1})	(km s^{-1})			
CS 30315-029	4541	1.07	−3.33	2.06	−169.2	+0.73	−0.31	−0.52
HE 0057-4541	5083	2.55	−2.32	1.67	13.4	+0.62	−0.74	+0.09
HE 0105-6141	5218	2.83	−2.55	1.66	3.8	+0.68	−0.50	+0.11
HE 0240-0807	4729	1.54	−2.68	1.96	−98.8	+0.73	−0.53	−0.43
HE 0516-3820	5342	3.05	−2.33	1.48	153.5	+0.67	−0.77	+0.30
HE 0524-2055	4739	1.57	−2.58	1.95	255.3	+0.49	−0.42	−0.33
HE 2229-4153	5138	2.47	−2.62	1.79	−139.6	+0.45	−0.73	+0.28

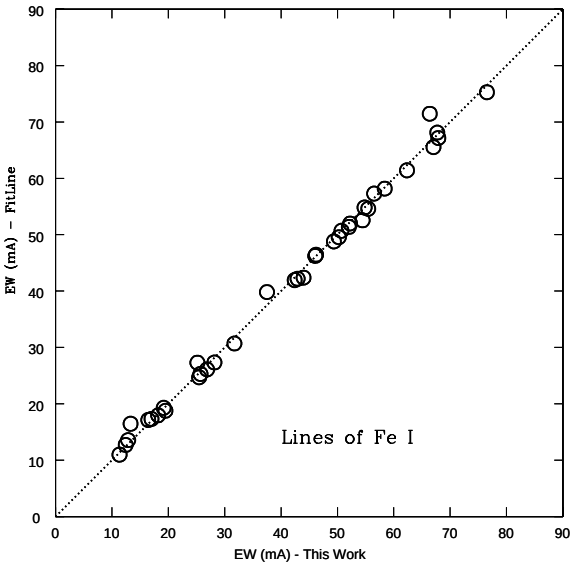

Fig. 1. Comparison of EWs measured for a set of Fe I lines in CS 30315-029 using the code developed in this work and EWs obtained with the code FitLine.

the EWs obtained with the present method and with Fitline for CS 30315-029, and demonstrates excellent agreement.

3. Abundance derivation

The OSMARCS 1D model atmosphere grid in local thermodynamic equilibrium (LTE) was employed (Gustafsson et al. 2003, 2008). We used the spectrum synthesis code Turbospectrum (Alvarez & Plez 1998), which includes proper treatment of diffusion in the UV, treatment of scattering in the blue and UV domain, molecular dissociative equilibrium, and collisional broadening by H, He, and H_2, following Anstee & O'Mara (1995), Barklem & O'Mara (1997), and Barklem et al. (1998). The calculations used the Turbospectrum molecular line lists (Alvarez & Plez 1998), and atomic line lists from the VALD2 compilation (Kupka et al. 1999).

3.1. Atmospheric parameters

3.1.1. Effective temperature derivation

The effective temperatures were previously derived by B05, based on 2MASS $(J-H)$ and $(J-K_S)$ colors, and calibrations by Alonso et al. (1999). We calculated photometric temperatures based on several colors: $(B-V)$, $(V-I)$, $(V-R)$, $(J-H)$, $(J-K)$ and $(V-K)$. Table 3 lists BVR_CI_C (Beers et al. 2007) and 2MASS JHK_S (Skrutskie et al. 2006) colors and magnitudes for the sample stars. Calibrations by Alonso et al. (1999) were applied, with reddening $E(B-V)$ computed with the Galactic Reddening and Extinction Calculator from the Infrared Processing and Analysis Center (IRSA) [2], which is based on Schlegel et al. (1998). The extinction laws given by Dean et al. (1978) and Rieke & Lebofsky (1985) were adopted.

The relations established by Fernie (1983) between the photometric systems of Johnson and Cousins were used, and the results agree well with those obtained from Bessell (1979). Colors from 2MASS were transformed into the Caltech (CIT) system, and from this into the TCS (Telescopio Carlos Sánchez) system, following the relations established by Carpenter (2001) and Alonso et al. (1998) (infrared flux method, IRFM). The transformations were also performed with the ESO photometric system in place of CIT, without significant differences in the final temperatures.

Table 4 lists the temperatures deduced from the different colors, as well as the adopted temperatures for each star. The adopted temperatures do not take into account the temperatures estimated from $(V-R)$, since they appear to be systematically higher than the other individual estimates. Table 4 provides the errors suggested by Alonso et al. (1999). Cayrel et al. (2004) adopted an error on E$(B-V)$ toward halo stars of about 0.02 mag, corresponding to a temperature error of about 60 K. This leads to a total error in the final temperature estimate of $\Delta T_{\rm eff} \sim 100$ K, which agrees well with B05.

3.1.2. Derivation of gravity and microturbulence velocity

An iterative method was adopted to derive estimates of the surface gravity, log g, and microturbulence velocity, ξ:

- By fixing the photometric $T_{\rm eff}$, together with [Fe/H] and ξ from B05, we calculated the ionization equilibrium for a series of models. We then chose the log g that minimizes ([Ti I/H]-[Ti II/H])+([Fe I/H]-[Fe II/H]).
- Adopting the newly derived log g and [Fe/H] values, ξ was chosen to minimize the dependence of [Fe I/H] on the equivalent width of the line.
- Using the newly derived ξ, [Fe/H], and log g were recomputed until stable values were obtained.

Fig. 2 shows an example of the dependence of [Fe I/H], [Fe II/H], [Ti I/H], and [Ti II/H] on log(EW/λ), and on the exci-

[2] http://irsa.ipac.caltech.edu/applications/DUST/

Table 2. Log of observations: coordinates, date of observation, exposure time, air mass at the beginning and at the end of the observation, geocentric and barycentric radial velocities.

Target	α(J2000)	δ(J2000)	Date	Exp.	Airmass	Airmass	RV_G	RV_B	Mean RV_B
				(sec)	Start	End	(km s^{-1})	(km s^{-1})	(km s^{-1})
CS 30315-029	23:34:26.5	−26:42:19	06.11.07	3600	1.063	1.006	−144.95	−169.43	−170.0
			08.11.07	3600	1.063	1.123	−145.39	−170.36	
			08.11.07	3600	1.127	1.322	−145.23	−170.31	
HE 0057-4541	00:59:59.2	−45:24:54	07.11.07	3600	1.143	1.080	30.93	14.15	13.7
			07.11.07	3600	1.072	1.081	30.79	13.90	
			07.11.07	3600	1.081	1.145	30.74	13.76	
			07.11.07	3600	1.146	1.281	30.89	13.82	
			08.11.07	3600	1.156	1.299	30.62	13.34	
			08.11.07	3600	1.303	1.564	30.67	13.31	
HE 0105-6141	01:07:38.0	−61:25:17	09.11.07	4500	1.425	1.683	20.09	5.33	5.3
HE 0240-0807	02:42:57.6	−07:54:35	07.11.07	3600	1.095	1.233	−96.02	−100.77	−101.8
			08.11.07	4500	1.232	1.631	−95.96	−101.31	
			10.11.07	3600	1.641	1.290	−96.44	−102.06	
			10.11.07	3600	1.287	1.120	−96.42	−102.14	
			10.11.07	3600	1.117	1.050	−96.17	−102.01	
			10.11.07	3600	1.045	1.069	−96.14	−102.15	
			10.11.07	3600	1.070	1.175	−95.89	−102.03	
			10.11.07	3600	1.178	1.408	−95.78	−102.04	
HE 0516-3820	05:18:12.9	−38:17:33	09.11.07	3600	1.056	1.144	148.20	154.38	154.4
HE 0524-2055	05:27:04.4	−20:52:42	07.11.07	3600	1.007	1.013	244.19	256.32	255.4
			07.11.07	3600	1.014	1.087	243.53	255.55	
			08.11.07	3300	1.030	1.116	243.65	255.31	
			10.11.07	3600	1.007	1.064	243.32	254.42	
HE 2229-4153	22:32:49.0	−41:38:25	08.11.07	2700	1.076	1.137	−113.97	−139.92	−138.5
			09.11.07	2700	1.046	1.066	−111.74	−137.66	
			09.11.07	2700	1.046	1.055	−111.94	−137.90	

Table 3. Identifications, magnitudes, and reddening.

Star	2MASS ID	(V)*	$(B-V)$*	$(V-R_C)$*	$(V-I_C)$*	(J)**	(H)**	(K_S)**	E$(B-V)$***
CS 30315-029	23342669-2642140	13.661±0.004	0.915±0.007	0.569±0.004	1.143±0.004	11.780±0.020	11.209±0.021	11.124±0.023	0.020
HE 0057-4541	00595927-4524534	14.829±0.005	0.699±0.009	0.441±0.007	0.890±0.007	13.376±0.021	12.970±0.026	12.877±0.031	0.016
HE 0105-6141	01073782-6125176	13.516±0.004	0.645±0.006	0.403±0.005	0.856±0.006	12.161±0.023	11.758±0.022	11.663±0.025	0.020
HE 0240-0807	02425772-0754354	14.971±0.005	0.896±0.012	0.524±0.007	1.082±0.008	13.213±0.022	12.707±0.032	12.625±0.031	0.025
HE 0516-3820	05181291-3817326	14.377±0.007	0.615±0.013	0.401±0.009	0.839±0.009	12.937±0.023	12.507±0.029	12.469±0.027	0.026
HE 0524-2055	05270444-2052420	14.013±0.004	0.878±0.007	0.526±0.005	1.076±0.005	12.256±0.026	11.747±0.026	11.623±0.019	0.045
HE 2229-4153	22324904-4138252	13.322±0.003	0.676±0.005	0.420±0.004	0.875±0.006	11.937±0.025	11.497±0.021	11.456±0.022	0.012

References. *: Broadband UBVR_CI$_C$ (subscript "C" indicates the Cousins system) from HK and Hamburg/ESO surveys (Beers et al. 2007); **: 2MASS (Cutri et al. 2003); ***: Infrared Processing and Analysis Center (IRSA, Schlegel et al. 1998).

Table 4. Temperatures and errors derived using the calibrations by Alonso et al. (1999) for several colors, and the final temperature adopted for each star. The error on the adopted temperature does not take into account the uncertainty on the reddening.

Star	$T_{\rm eff}(B-V)$	$T_{\rm eff}(V-I)$	$T_{\rm eff}(V-R)$	$T_{\rm eff}(J-H)$	$T_{\rm eff}(J-K)$	$T_{\rm eff}(V-K)$	Adopted $T_{\rm eff}$
CS 30315-029	4703±96	4523±125	4959±150	4383±170	4622±125	4621±25	4570±53
HE 0057-4541	5104±167	5069±125	5372±150	5158±170	5153±125	5237±40	5144±60
HE 0105-6141	5273±167	5176±125	5638±150	5156±170	5167±125	5398±40	5234±60
HE 0240-0807	4689±96	4656±125	5064±150	4707±170	4847±125	4802±40	4740±53
HE 0516-3820	5400±167	5244±125	5633±150	5067±170	5302±125	5333±40	5269±60
HE 0524-2055	4736±96	4725±125	5096±150	4736±170	4734±125	4813±40	4749±53
HE 2229-4153	5146±167	5097±125	5529±150	4966±170	5218±125	5354±40	5156±60

tation potential of the lines for HE 0240-0807. With the adopted parameters, the Fe I and Fe II lines (black and red dots, respectively) lead to the same iron abundance (the same is observed for the Ti I and Ti II lines). Our choice of $T_{\rm eff}$ (photometric temperature) is also supported by the fulfilled ionization and excitation equilibria for [Fe/H] and [Ti/H], as shown in Fig. 2. In this check of consistency, the Fe I lines with an excitation potential lower than 1.4 eV were excluded, because they are severely affected by NLTE effects (see Cayrel et al. 2004).

The adopted parameters are given in Table 5. Typical uncertainties are $\Delta\log g = 0.1$ dex and $\Delta\xi = 0.2$ km s^{-1} (e.g. Cayrel et al. 2004). As pointed out by Cayrel et al. (2004), the log g val-

Table 5. Adopted atmospheric parameters.

Star	$T_{\rm eff}$	log g	[Fe/H]	ξ
	(K)	[cgs]		(km s^{-1})
CS 30315-029	4570	0.99	−3.40	2.22
HE 0057-4541	5144	2.73	−2.40	1.79
HE 0105-6141	5234	2.91	−2.57	1.42
HE 0240-0807	4740	1.50	−2.86	2.27
HE 0516-3820	5269	2.17	−2.51	1.48
HE 0524-2055	4749	1.53	−2.77	2.20
HE 2229-4153	5156	2.67	−2.62	1.63

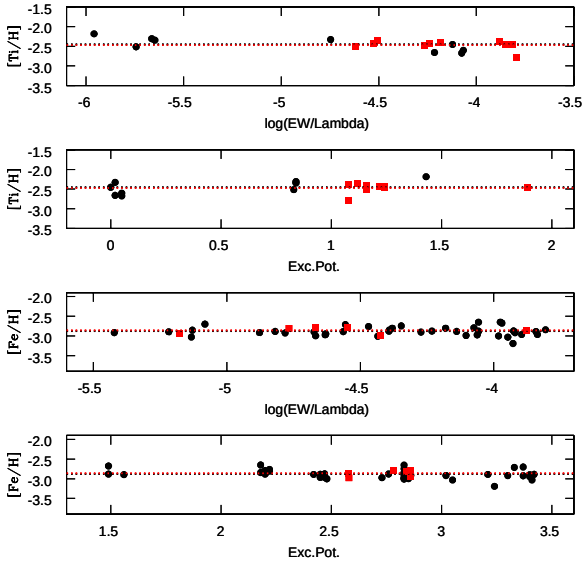

Fig. 2. Excitation and ionization equilibria of Ti and Fe lines, resulting from the new set of atmospheric parameters for HE 0240-0807. The black dots are the abundances obtained from Ti I and Fe I lines, and the red squares are those from Ti II and Fe II lines; the black dotted lines represent the average metallicity from the neutral species, and the red dotted lines represent the average metallicity from the ionized species.

ues may be affected by NLTE effects (overionization), and by uncertainties in the oscillator strengths of the Fe and Ti lines. Comparing these results with the parameters from B05, the average difference (and dispersion as the standard deviation) in the temperatures is $\Delta T_{\rm eff}$ = 10(24) K. For surface gravity, metallicity, and microturbulence, the results are $\Delta\log g$ = −0.08 (0.23) [cgs], Δ[Fe/H] = −0.10 (0.07) dex and $\Delta\xi$ = 0.06 (0.17) km s^{-1} . The results show a good consistency between the two sets of parameters.

3.2. Derived abundances

The elemental abundances were derived using equivalent widths for lines of titanium and iron. A line-by-line fitting was carried out for the other elements, with special attention given to the molecular bands (CH, CN, NH), to the lines affected by hyperfine splitting, or that were severely blended, and to all the lines of the heavy elements.

Synthetic spectra were convolved with Gaussian profiles that take into account, in combination, the effects of macroturbulence, rotational, and instrumental broadening. This analysis is very sensitive to the determination of the continuum. We determined a local continuum around each line before computing the χ^2 between computed and observed spectra, using the synthetic spectra as reference.

The position and intensity of the telluric lines were computed by means of the line-by-line radiative transfer model code (LBLRTM; Clough et al. 2005), using the high-resolution transmission molecular absorption database (HITRAN; Rothman et al. 2009). We used the same transmission, $T_0(\lambda)$, computed for a standard atmosphere by Chen et al. (2013) for the altitude of the Observatory, modified to take into account the airmass variations from star to star. Stellar lines that are severely blended by telluric lines were excluded.

The final abundance estimates for each element are the mean of abundances from all individual lines; the internal (observational) uncertainty corresponds to the standard deviation of the distribution of estimates. Table 6 presents the LTE abundances A(X)[3] and the [X/Fe] abundance ratios of all studied elements for each star of the sample. The complete line list as well as abundance values from individual lines can be found in Table A.2.

3.3. Uncertainties on the derived abundances

We adopted typical errors in the atmospheric parameters: $\Delta T_{\rm eff}$ = 100 K, $\Delta\log g$ = 0.1 dex, and $\Delta\xi$ = 0.2 km s^{-1}. It is possible to estimate the abundance uncertainties that arise from each of these three sources independently. However, the quadratic sum of the various sources of uncertainties is probably not the best way to estimate the total error budget, since the stellar parameters are not independent of each other, which adds significant covariance terms to this calculation.

To solve this, we created a new atmospheric model with a 100 K lower temperature, determining the corresponding surface gravity and microturbulent velocity by the traditional method. The difference between this model and the nominal model are expected to represent the total error budget arising from the stellar parameters. The final error is the sum of the uncertainty from the atmospheric parameters with the observational error. Table 7 shows the final values in CS 30315-029 as an example.

4. Results

4.1. Light and iron-peak elements

4.1.1. Lithium

The atmospheres of cool giant stars are Li-depleted. This is expected, since Li is destroyed at temperatures in excess of 2.5×10^{6}K. Such temperatures are reached in the inner atmospheric layers, which are mixed by convection into the outer atmosphere of the star.

HE 0057-4541 and HE 0105-6141 show very clear line profiles at 6707 Å. The final lithium abundances are A(Li) = +1.14 and A(Li) = +1.16, respectively. Fig. 3 shows the fit used for both cases, where the blue dotted lines are the synthetic spectra computed with the abundances indicated in the figure, and the red solid lines are the abundances from the best fits.

The lithium line profile of HE 0516-3820 is weak, but we derived an abundance of A(Li) = +0.96. The line profile of

[3] We adopted the notation A(X) = log (X) = log n(X)/n(H) + 12, with n = number density of atoms

Table 6. LTE abundances.

Element	A(X)	[X/Fe]	A(X)	[X/Fe]	A(X)	[X/Fe]	A(X)	[X/Fe]	A(X)	[X/Fe]	A(X)	[X/Fe]	A(X)	[X/Fe]
	CS 30315-029		HE 0057-4541		HE 0105-6141		HE 0240-0807		HE 0516-3820		HE 0524-2055		HE 2229-4153	
Fe I*	4.07	−3.45	5.16	−2.36	4.94	−2.58	4.64	−2.88	5.02	−2.50	4.76	−2.76	4.89	−2.63
Fe II*	4.08	−3.44	5.16	−2.36	4.96	−2.56	4.66	−2.86	5.02	−2.50	4.76	−2.76	4.89	−2.63
Li I	—	—	1.14	+2.47	1.16	+2.71	—	—	0.96	+2.43	—	—	0.98	+2.58
C	5.00	−0.06	6.58	+0.44	6.10	+0.17	5.20	−0.43	6.35	+0.35	5.84	+0.10	6.40	+0.53
N(CN)	5.60	+1.19	5.65	+0.15	—	—	5.70	+0.72	5.70	+0.34	5.95	+0.85	—	—
N(NH)	5.95	+1.54	5.70	+0.20	<5.20	< −0.08	6.05	+1.07	5.80	+0.44	6.20	+1.10	5.35	+0.12
Mg	4.75	+0.65	5.65	+0.47	5.42	+0.45	5.23	+0.57	5.55	+0.51	5.60	+0.82	5.55	+0.64
Al	2.68	−0.35	3.50	−0.61	3.20	−0.70	3.26	−0.34	3.30	−0.67	3.40	−0.31	3.25	−0.59
Si	4.80	+0.72	5.94	+0.78	5.64	+0.69	5.30	+0.65	5.45	+0.43	5.37	+0.61	5.48	+0.59
S	4.33	+0.61	5.35	+0.55	5.25	+0.66	4.95	+0.66	5.35	+0.69	5.08	+0.68	5.05	+0.52
K	2.60	+0.93	3.30	+0.55	2.92	+0.38	2.95	+0.71	3.18	+0.57	3.27	+0.92	3.25	+0.77
Ca	3.32	+0.43	4.33	+0.37	4.17	+0.41	3.82	+0.37	4.23	+0.40	4.00	+0.44	4.13	+0.44
Sc	−0.36	−0.02	0.84	+0.10	0.77	+0.24	0.38	+0.16	0.75	+0.15	0.42	+0.09	0.62	+0.15
Ti I	1.86	+0.40	2.95	+0.42	2.81	+0.49	2.45	+0.43	2.74	+0.34	2.54	+0.40	2.67	+0.41
Ti II	1.80	+0.35	2.96	+0.42	2.83	+0.51	2.43	+0.41	2.77	+0.38	2.53	+0.39	2.66	+0.39
V I	0.32	−0.24	1.57	−0.07	1.32	−0.10	1.12	−0.01	1.40	−0.10	1.22	−0.02	1.35	−0.01
V II	0.53	−0.03	1.87	+0.23	1.65	+0.22	1.37	+0.24	1.69	+0.19	1.34	+0.10	1.51	+0.14
Cr	1.78	−0.41	3.06	−0.21	2.83	−0.24	2.30	−0.47	3.05	−0.09	2.44	−0.44	2.75	−0.25
Mn	1.58	−0.35	2.78	−0.23	2.37	−0.43	2.07	−0.43	2.73	−0.14	2.26	−0.35	2.42	−0.32
Co	1.74	+0.26	2.86	+0.30	2.80	+0.45	2.29	+0.24	2.81	+0.40	2.45	+0.29	2.63	+0.34
Ni	2.78	−0.01	3.79	−0.08	3.75	+0.09	3.31	−0.05	3.85	+0.12	3.39	−0.08	3.70	+0.10
Sr	−0.84	−0.32	0.80	+0.24	0.64	+0.29	−0.08	−0.13	0.65	+0.23	0.15	−0.01	0.57	+0.28
Y	−1.45	−0.22	−0.30	−0.14	−0.39	−0.03	−0.72	−0.06	−0.14	+0.16	−0.71	−0.16	−0.47	−0.05
Zr	−0.77	+0.10	0.54	+0.32	0.21	+0.20	−0.03	+0.26	0.51	+0.44	0.11	+0.30	0.22	+0.27
Mo	< −1.15	< +0.37	—	—	—	—	—	—	—	—	< −0.35	< +0.49	—	—
Ru	−0.95	+0.65	0.24	+0.76	—	—	< −0.20	< +0.83	—	—	−0.15	+0.77	< −0.13	< +0.66
Pd	< −1.10	<0.68	—	—	—	—	—	—	—	—	—	—	< −0.60	< +0.37
Ba	−1.10	+0.17	−0.22	−0.03	−0.25	−0.15	−0.50	+0.20	−0.27	+0.06	−0.63	−0.04	−0.65	−0.19
La	−2.06	+0.24	−1.00	+0.22	−1.15	+0.28	−1.44	+0.29	−1.18	+0.18	−1.57	+0.05	−1.58	−0.08
Ce	−1.65	+0.18	−0.48	+0.27	< −0.85	< +0.11	−1.00	+0.26	−0.44	+0.45	−1.22	−0.07	−1.05	−0.03
Pr	−2.13	+0.56	< −1.09	<0.51	< −0.85	< +0.97	−1.52	+0.60	< −0.88	< +0.87	−1.62	+0.39	−1.50	+0.37
Nd	−1.56	+0.44	−0.56	+0.35	−0.53	+0.59	−0.93	+0.50	−0.46	+0.60	−1.03	+0.28	−1.00	+0.19
Sm	−1.76	+0.68	−0.97	+0.40	−0.80	+0.77	−1.19	+0.69	< −0.46	< +1.04	−1.42	+0.35	−1.33	+0.31
Eu	−2.24	+0.68	−1.27	+0.58	−1.53	+0.52	−1.58	+0.78	−1.34	+0.64	−1.75	+0.50	−1.72	+0.39
Gd	−1.85	+0.48	−0.85	+0.40	< −0.90	< +0.56	−1.09	+0.67	−1.12	+0.27	−1.38	+0.27	−1.33	+0.20
Tb	−2.40	+0.76	—	—	—	—	< −1.78	< +0.82	—	—	< −1.95	< +0.53	—	—
Dy	−1.62	+0.69	−0.62	+0.61	−0.98	+0.46	−1.03	+0.71	−0.73	+0.65	−1.12	+0.51	−1.15	+0.35
Ho	−2.38	+0.56	−1.32	+0.53	—	—	−1.63	+0.74	< −1.00	< +0.99	−1.80	+0.45	−1.90	+0.22
Er	−1.75	+0.73	−0.78	+0.63	—	—	−1.22	+0.69	< −0.78	< +0.76	−1.27	+0.53	−1.17	+0.50
Tm	−2.72	+0.59	< −1.46	< +0.77	—	—	< −1.86	< +0.87	—	—	—	—	< −1.93	< +0.57
Yb	−1.98	+0.60	−0.95	+0.55	−1.22	+0.49	−1.25	+0.76	−0.97	+0.67	−1.58	+0.32	−1.53	+0.24
Os	< −1.00	< +1.08	—	—	—	—	< −0.43	< +1.09	—	—	—	—	—	—
Ir	< −0.74	< +1.32	<0.01	< +0.99	—	—	< −0.20	< +1.29	—	—	< −0.45	< +0.93	—	—
Th	−2.45	+0.91	< −1.40	< +0.88	—	—	< −1.92	< +0.87	—	—	< −2.12	< +0.56	—	—

References. *: [X/H] is used in place of [X/Fe].

HE 2229-4153 yields an upper limit of A(Li) < +0.98. As expected, all the values determined are below the lithium plateau for warm dwarf halo stars, and correspond to the Li abundance observed in giant stars after the first dredge-up, but before the onset of extra mixing (Spite et al. 2005). A low NLTE correction of ∼0.05 dex on the Li abundance is given by Lind et al. (2009) for parameters similar to those of the present sample.

For CS 30315-029 and HE 0524-2055, the lithium line is not visible (A(Li) < 0.0). These giants are cool and have very probably undergone extra-mixing events, as confirmed by their very low value of [C/N]: [C/N] = −1.07 for CS 30315-029 and [C/N] = −0.75 for HE 0524-2055 (see Spite et al. 2005). For HE 0240-0807, no spectra were available in the lithium line region.

4.1.2. Carbon and nitrogen

The carbon abundance was derived from the CH $A^2\Delta$-$X^2\Pi$ (0,0) transitions (G-band), with lines present in the range 4290 Å - 4310 Å, and the bandhead at ∼4310 Å. Fig. 4 shows an example of fit (upper panel) for HE 2229-4153; and one can see that this region is almost devoid of atomic lines. Beers & Christlieb (2005) defined carbon-enhanced stars as having [C/Fe] > +1.0. However, in this work we prefer the definition for the carbon-enhancement phenomenon in metal-poor stars as presented by Aoki et al. (2007; [C/Fe] > +0.7), which also takes into account that the surface abundance of carbon in evolved stars will in general be lower than it was when the star was in an earlier evolutionary stage as a consequence of mixing events. The lower panel in Fig. 4 shows carbon abundances obtained in this work (red circles) and the criterion for carbon-enhanced stars as defined by Aoki et al. (2007) (dashed blue line). The previous results from B05 are also presented for comparison purposes (crosses). The new results, obtained from our high-resolution spectra, confirm that none of the sample stars are carbon-enhanced.

The nitrogen abundance was derived from the (0,0) bandhead of the blue CN $B^2\Sigma$-$X^2\Sigma$ at 3883 Å. However, this line is weak and not detectable for HE 0105-6141 and HE 2229-4153. We also used lines of the NH $A^3\Pi_i$–$X^3\Sigma_-$ band, with a bandhead at 3360 Å. The NH lines give the nitrogen abundance with a dependence on the C abundance only through dissociative equilibrium, but not directly in the line intensity (as for CN lines).

Figure 5 compares the results for our sample stars (black dots), obtained with CN and NH, compared with the results from Spite et al. (2005) (blue dots) for the LP "First Stars". Spite et al. (2005) pointed out a systematic difference of 0.4 dex between the two indicators, and the present results confirm this discrepancy, as shown by the red solid line in Fig. 5. The reason for this difference is not clear, but it might be related to molecular constants and also to different 3D effects on the NH and CN lines. The molecular lines are indeed formed very close to the surface, a region where 3D effects can be important. The two carbon-rich

Table 7. Observational and atmospheric errors in CS 30315-029, as well as the final uncertainties.

Element	Δ_{obs}	Δ_{atm}	Δ_{final}	$\Delta_{final[X/Fe]}$
	(dex)	(dex)	(dex)	(dex)
Fe I	0.09	0.09	0.13	–
Fe II	0.06	0.06	0.09	–
C	0.10	0.16	0.19	0.22
N	0.10	0.10	0.14	0.21
Mg	0.07	0.09	0.11	0.17
Al	0.10	0.12	0.16	0.20
Si	0.10	0.02	0.10	0.16
S	0.10	0.12	0.16	0.20
K	0.10	0.05	0.11	0.18
Ca	0.07	0.02	0.07	0.14
Sc	0.05	0.04	0.06	0.16
Ti I	0.11	0.14	0.17	0.21
Ti II	0.07	0.09	0.12	0.17
V I	0.10	0.07	0.12	0.16
V II	0.06	0.07	0.09	0.14
Cr	0.01	0.02	0.02	0.11
Mn	0.10	0.07	0.12	0.17
Co	0.10	0.04	0.11	0.17
Ni	0.10	0.02	0.10	0.15
Sr	0.10	0.06	0.12	0.17
Y	0.02	0.07	0.07	0.13
Zr	0.07	0.06	0.09	0.14
Ru	0.10	0.10	0.14	0.19
Ba	0.10	0.02	0.10	0.16
La	0.05	0.07	0.09	0.14
Ce	0.10	0.10	0.14	0.18
Pr	0.03	0.08	0.09	0.14
Nd	0.05	0.05	0.07	0.13
Sm	0.08	0.07	0.10	0.16
Eu	0.05	0.05	0.07	0.13
Gd	0.10	0.05	0.11	0.16
Tb	0.10	0.10	0.14	0.20
Dy	0.07	0.12	0.14	0.18
Ho	0.10	0.08	0.13	0.19
Er	0.10	0.08	0.13	0.18
Tm	0.10	0.07	0.12	0.17
Yb	0.10	0.07	0.12	0.19
Th	0.10	0.10	0.14	0.18

stars from Spite et al. (2005) are identified in Fig. 5, CS 22949-037 ([C/Fe] = +1.21) and CS 22892-052 ([C/Fe] = +0.93).

4.1.3. The α-elements: Mg, Si, S, Ca, and Ti

We derived abundances of magnesium, calcium, and titanium using lines of Mg I, Ca I, Ti I, and Ti II; Table A.2 reports the abundances for individual lines (see Table A.1 for Ti), and the averaged results are shown in Table 6. Fig. 6 shows the fit for the Ca I 4289.37 Å line for HE 0105-6141 (upper panel) and for the Ca I 4318.65 Å line for HE 2229-4153 (lower panel).

Andrievsky et al. (2010) presented NLTE computations for Mg abundances in stars observed in the framework of the LP "First Stars" and found an average correction of Δ_{NLTE} = +0.19 dex[4]. To estimate the 3D corrections on the results, we used hydrodynamical models computed with the code CO5BOLD (Freytag et al. 2002, 2012) with $T_{\rm eff}$ = 5000 K, log g = 2.5 [cgs], and two different metallicities, [Fe/H] = −2 and [Fe/H] = −3. The plane-parallel 1D$_{LHD}$ model was used as

[4] Δ_{NLTE} = A(X) $_{NLTE}$ - A(X)$_{LTE}$

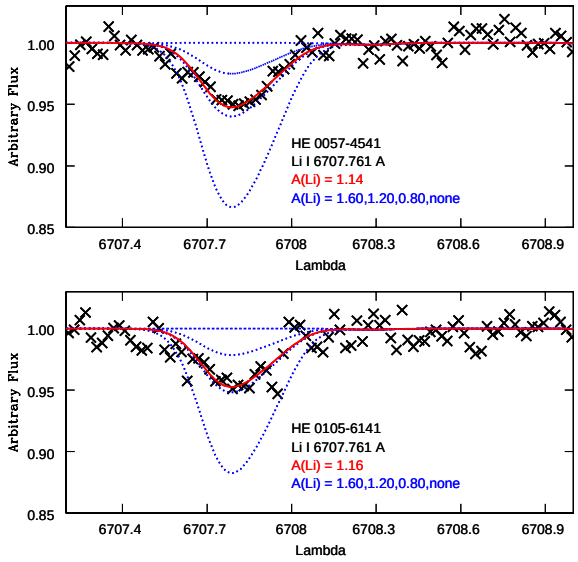

Fig. 3. Li abundances for HE 0057-4541 (upper panel) and HE 0105-6141 (lower panel). Observations (crosses) are compared with synthetic spectra computed with different abundances (blue dotted lines), as well as with the adopted abundances (red solid lines).

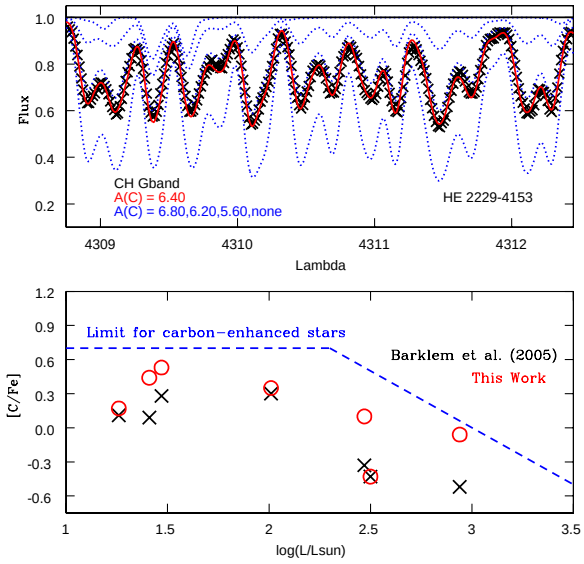

Fig. 4. Upper panel: carbon abundance for HE 2229-4153, derived from the CH $A^2\Delta$-$X^2\Pi$ (0,0) transitions (G-band). Symbols are the same as in Fig. 3. Lower panel: comparison of the results obtained in this work (red circles) with those previously obtained by Barklem et al. (2005) (crosses). The dashed blue line corresponds to the limit for carbon-enhanced stars, as defined by Aoki et al. (2007).

reference model, computed with the LHD code, which shares the microphysics and opacity with the CO5BOLD code. The 3D correction is defined as A(3D)-A(1D$_{LHD}$) (see details in Caffau et al. 2011). The line-formations were computed with Linfor3D[5]

[5] http://www.aip.de/Members/msteffen/linfor3d/files/linfor3d-manual

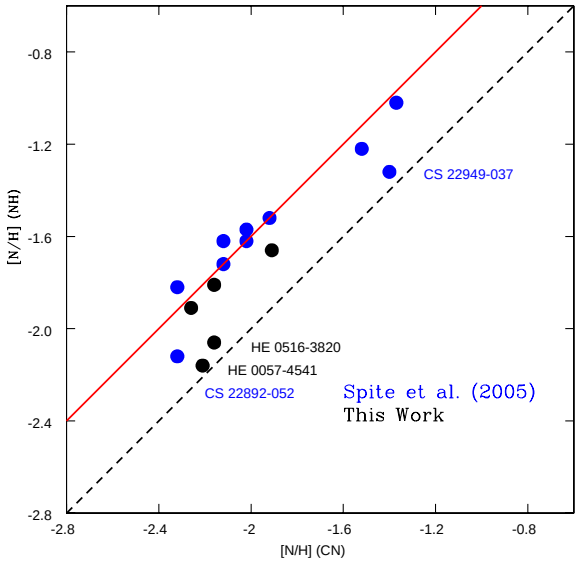

Fig. 5. Abundance ratios for [N/H] obtained from the molecular bands of CN and NH in the present sample (black dots), compared with the results from Spite et al. (2005) (blue dots). The one-to-one relation is shown by a dashed black line. The solid red line indicates a correlation offset by 0.4 dex.

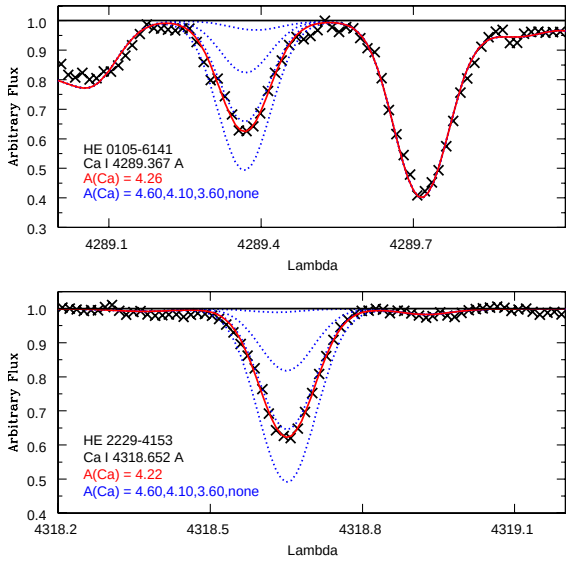

Fig. 6. Ca abundances from the Ca I 4289.37 Å line for HE 0105-6141 (upper panel), and from the Ca I 4318.65 Å line for HE 2229-4153 (lower panel). Symbols are the same as in Fig. 3.

for the Mg I lines studied in this work. The results obtained are $\Delta_{3D} = +0.09$ dex and $\Delta_{3D} = -0.04$ dex for [Fe/H] = −2 and [Fe/H] = −3, respectively. For further discussions about the NLTE computation and 3D correction of the Ca abundances see Spite et al. (2012).

In the visible region, the main indicators of silicon abundance are the Si I line at 3905.52 Å, which in giants is too severely blended by a CH line, and the Si I line at 4102.94 Å, located in the red wing of the Hδ line. We therefore used spectrum synthesis of this Si line, taking into account the hydrogen line. Fig. 7 shows the fits obtained for CS 30315-029 (upper panel) and HE 2229-4153 (lower panel). Using the same approach as described for Mg to estimate the 3D effect on the Si abundances, the results obtained for the 4102.94 Å line are $\Delta_{3D} = +0.04$ dex and $\Delta_{3D} = -0.09$ dex, with [Fe/H] = −2 and [Fe/H] = −3, respectively.

Figures 8 and 9 compare the LTE abundance trends of the α-elements obtained in this work (red stars) and in the ESO LP "First Stars" (Cayrel et al. 2004; Bonifacio et al. 2009; black crosses). The NLTE and 3D corrections are listed in the text for reference only. The r-I and r-II stars are represented by blue and magenta star symbols, respectively. The α-elements are enhanced for both sets of stars and the trends are very similar. We remark in particular that the scatter of [Mg/Fe] from star to star is larger than the scatter of [Ca/Fe] and [Ti/Fe], as is generally observed.

The abundance of sulfur was derived from the S I lines at 9212.86 Å, 9228.09 Å, and 9237.54 Å. This wavelength region suffers from CCD fringes that affect the continuum placement, and the definition of a local continuum is mandatory. Another difficulty arises from the telluric H_2O lines present in the region, which were taken into account according to the method described in Sect. 3.2. Sulfur transitions that are severely blended by telluric lines were not considered in the final result. In addition, the S I 9228.09 Å line is located on the blue side of the Paschen Pζ wing, which was included in the synthesis. Fig. 10 shows the result for CS 30315-029 (upper panel). One can also see a telluric line in the red wing of the Pζ, represented by the green solid line.

Spite et al. (2011) presented S abundances for 33 metal-poor stars observed in the framework of the LP "First Stars," taking into account NLTE calculations and 3D corrections. As an estimate, the average correction $\Delta_{NLTE+3D} = -0.23$ dex from Spite et al. (2011) was applied to the present results. Fig. 10 presents in the lower panel the comparison of our final abundaces with the results obtained by Spite et al. (2011). The formation of sulfur remains controversial, and the trend of [S/Fe] versus [Fe/H] in the early Galaxy is still debated. The result shows that this element presents an α-element-like behavior, and the abundances derived in the present work follow the general trend.

It is important to note that the results do not come from a full 3D NLTE computation, and the NLTE and 3D corrections were obtained separately. It is well-known that the two effects combine in a clearly nonlinear way (see Gustafsson 2009 and references therein), but only diagnostic works have been done so far with the complete approach for few elements. In this sense, the corrections we present should be regarded as estimates.

4.1.4. Odd-Z elements: Al, K, and Sc

The published data from the HERES survey (B05) do not exhibit significant differences between r-I and r-II stars for the abundances of the normal elements (i.e., the non neutron-capture elements). Figs. 8 and 9 show that the same is true for the ESO LP "First Stars" data. The only element that seems to differ slightly between the stellar groups is the odd-Z element aluminum, thus this element was measured in our new high-resolution spectra as well. In addition, we decided to measure the odd-Z element potassium. For both S and K, spectra in the near-infrared region are needed, which were included in the observation program of the present work.

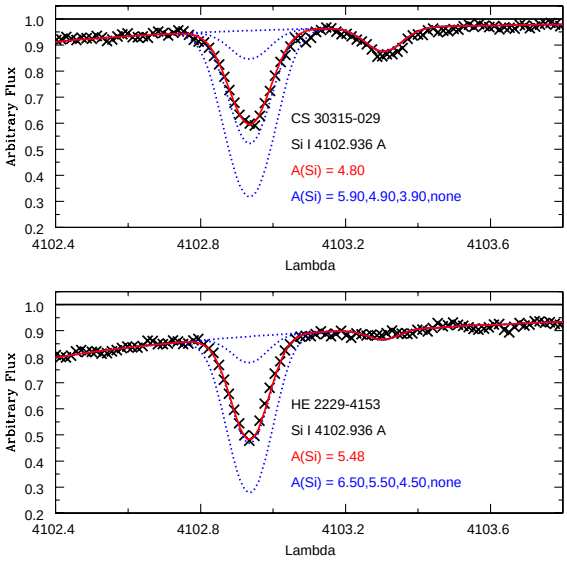

Fig. 7. Si abundances from the Si I 4102.94 Å line for CS 30315-029 (upper panel), and for HE 2229-4153 (lower panel). Symbols are the same as in Fig. 3.

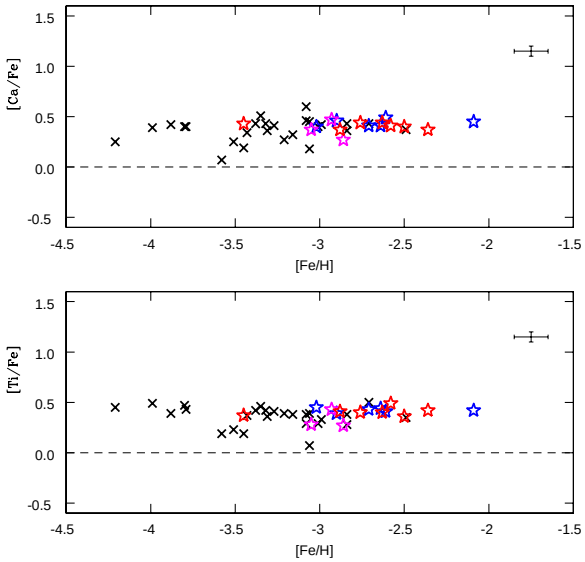

Fig. 9. Comparison of the abundance ratios [Ca/Fe] (upper panel) and [Ti/Fe] (lower panel) obtained in this work with the LTE results from Cayrel et al. (2004). Symbols are the same as in Fig. 8.

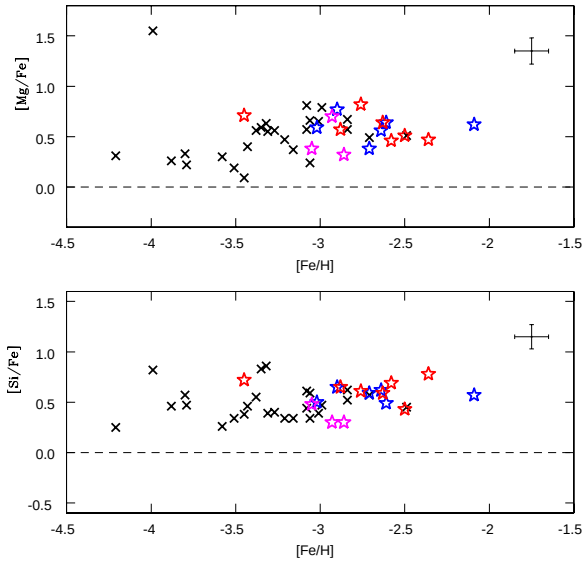

Fig. 8. Comparison of the abundance ratios for [Mg/Fe] (upper panel) and [Si/Fe] (lower panel), obtained in this work (red stars) with the LTE results from Cayrel et al. (2004): black crosses for normal stars; magenta for r-II stars; and blue for r-I stars. The average of the error bars is indicated in the figure.

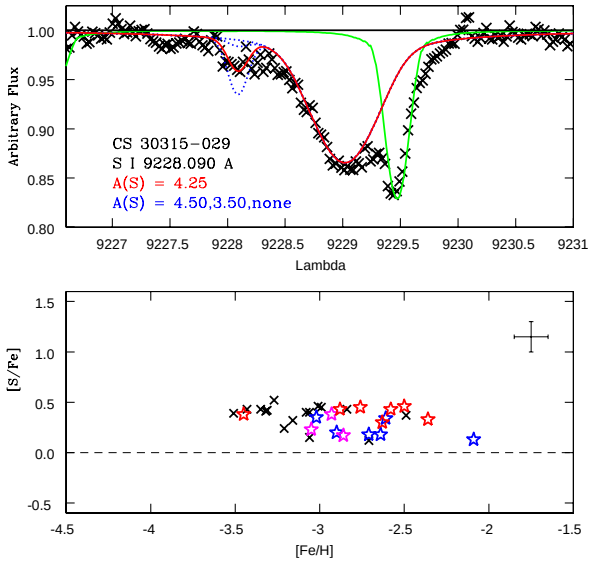

Fig. 10. Upper panel: S abundances from the S I 9228.09 Å line for the star CS 30315-029. The green solid lines are the synthetic telluric transmission. Lower panel: comparison of the abundance ratio [S/Fe] obtained in this work with the results from Spite et al. (2011). Symbols are the same as in Fig. 8.

The Al abundances were derived from the Al I 3944.01 Å and Al I 3961.52 Å doublet lines. A blend with CH lines for the Al I 3944.01 Å line was taken into account, but in some stars the contribution of the molecular lines is strong, so we preferred to adopt only the Al I 3961.52 Å line in the final abundances. Fig. 11 shows the results for CS 30315-029 (upper panel) and HE 0105-6141 (lower panel).

The K abundances were derived from the K I 7664.91 Å line and the K I 7698.97 Å doublet lines. Even correcting for the telluric lines, for half of our sample stars the K I 7664.91 Å line was severely compromised and was discarded, as shown in Fig. 12 (upper panel) for HE 0057-4541. For HE 0516-3820, it was possible to use the same line, and the result is shown in Fig. 12 (lower panel).

Given that the abundances were measured from resonance lines, which are very sensitive to NLTE effects, it is important to correct for this effect. Cayrel et al. (2004) adopted a constant correction for all the stars as a rough estimate: for Al a correction of +0.65 dex from Baumüller & Gehren (1997) and Norris et al.

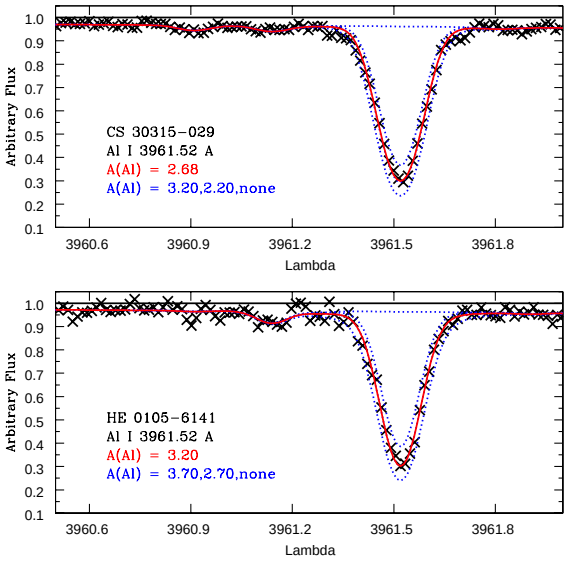

Fig. 11. Al abundances from the Al I 3961.52 Å line for CS 30315-029 (upper panel), and for HE 0105-6141 (lower panel). Symbols are the same as in Fig. 3.

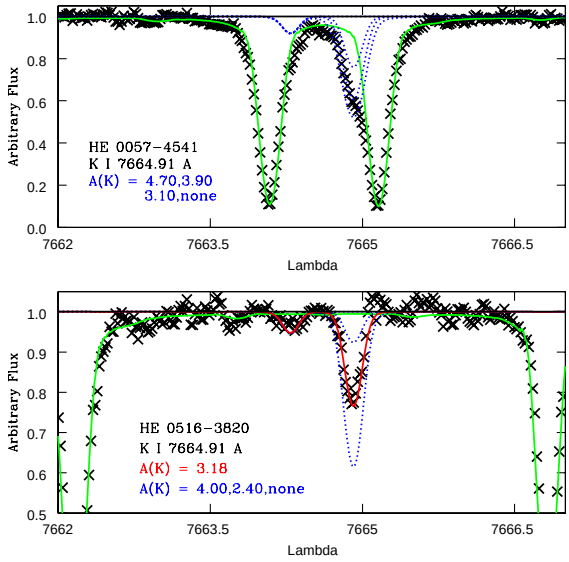

Fig. 12. K abundances from the K I 7664.91 Å line for HE 0057-4541 (upper panel), and for HE 0516-3820 (lower panel). Symbols are the same as in Fig. 3. The green solid lines are the synthetic telluric transmission features.

(2001), and for K, a correction of −0.35 dex from Ivanova & Shimanskii (2000).

Andrievsky et al. (2008) have computed the NLTE Al abundances in the LP "First Stars" sample. The NLTE corrections Δ_{NLTE} behavior with effective temperature, surface gravity, and metallicity of the model is also provided (see Fig. 2 in their paper), from which we estimate Δ_{NLTE} for the present sample. The LTE Al abundances in Table 6 must be corrected by Δ_{NLTE} = +0.20 dex,+0.65 dex,+0.75 dex,+0.25 dex, +0.65 dex,+0.30 dex, and +0.75 dex for CS 30315-029, HE 0057-4541, HE 0105-6141, HE 0240-0807, HE 0516-3820, HE 0524-2055, and HE 2229-4153, respectively. Applying our computations to estimate the 3D corrections to Al abundances, the results obtained with the Al I 3961.52 Å line are Δ_{3D} = −0.02 dex and Δ_{3D} = −0.33 dex, with metallicities of [Fe/H] = −2 and [Fe/H] = −3, respectively, showing that this effect becomes strong in extremely metal-poor stars.

Takeda et al. (2009) reanalyzed the K abundances from the EWs of the LP "First Stars," showing that the NLTE corrections systematically decrease with decreasing metallicity: $\Delta_{NLTE} \sim -0.3$ dex at [Fe/H] ∼ −2.5 dex and $\Delta_{NLTE} \sim -0.2$ dex at [Fe/H] ∼ −4 dex. Andrievsky et al. (2010) studied the same sample, and their results present small differences as compared with Takeda et al. (2009) because a direct fit of the profiles was carried out instead of employing EWs. The spectral synthesis was also used in the present work, so the NLTE corrections were adopted from Andrievsky et al. (2010), and to estimate the effect Δ_{NLTE} on our sample we used a regression line as a function of metallicities based on their results, $\Delta_{NLTE} = -0.125 \times [\mathrm{Fe/H}] - 0.6$. This method is a first rough estimate, because it is known that the temperature and gravity also play a role in the calculations.

Fig. 13 compares the NLTE results in this work for the abundance ratios [Al/Fe] and [K/Fe] with the literature (see text above). The 3D corrections are listed in the text for reference only. An excellent agreement was obtained for Al, and again no significant global difference was clearly found for the r-I stars relative to r-II stars (or the normal stars). Within the r-I stars, the

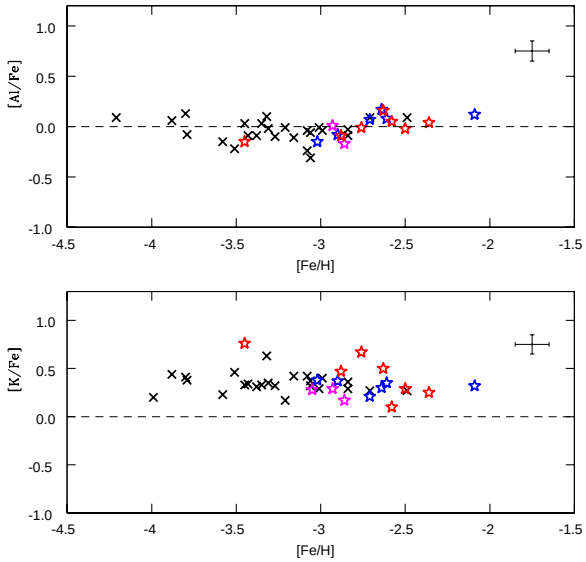

Fig. 13. Comparison of the abundance ratios for [Al/Fe] and [K/Fe] obtained in this work with the results from Cayrel et al. (2004). NLTE corrections were taken into account. Symbols are the same as in Fig. 8.

abundances of S and Al are remarkably constant, while the K abundances are more widely scattered. Indeed, some r-I stars analyzed in our sample seem to present higher K abundances than the general trend. The difference might arise because of the difficulty in measuring this element, or because of the rough NLTE correction assumed above.

The scandium abundances were derived from 9 Sc II lines. Fig. 14 shows the Sc II 4246.82 Å line for HE 2229-4153 (upper panel). The results agree with the abundances obtained in Cayrel et al. (2004), as shown in Fig. 14 (lower panel). Compared with

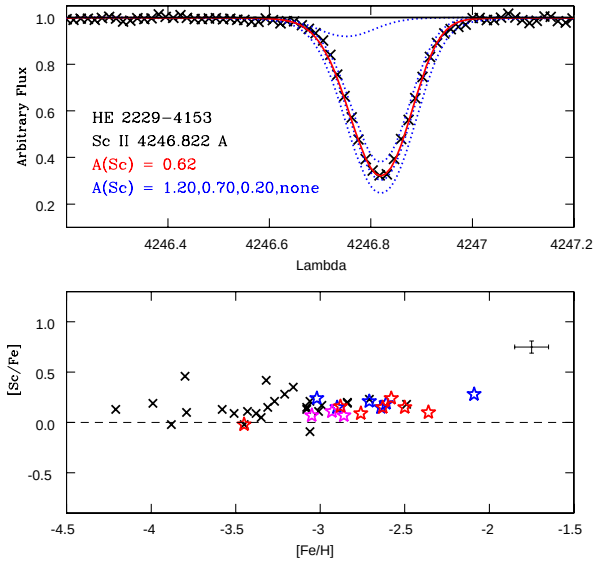

Fig. 14. Upper panel: Sc abundances from the Sc II 4246.82 Å line for HE 2229-4153. Symbols are the same as in Fig. 3. Lower panel: comparison of the abundance ratio [Sc/Fe] obtained in this work with the LTE results from Cayrel et al. (2004). Symbols are the same as in Fig. 8.

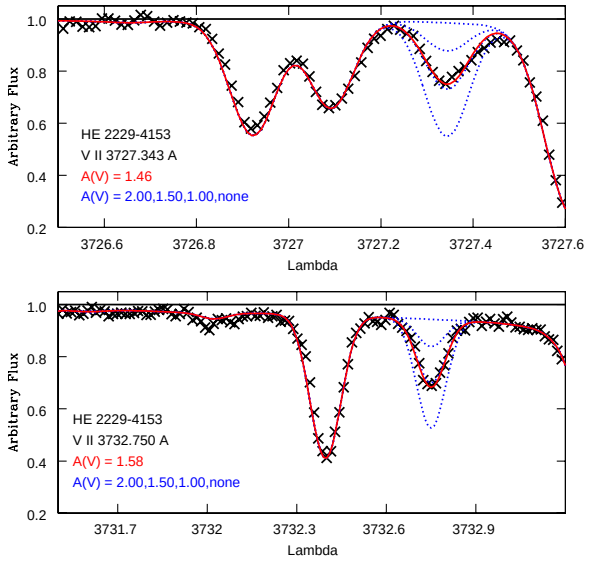

Fig. 15. V abundances from the V II 3727.34 Å line (upper panel) and line V II 3732.75 Å line (lower panel) for HE 2229-4153. Symbols are the same as in Fig. 3.

the other odd-Z elements (Al and K), the scatter in Sc results is much lower. Based on the Sc II lines located at 4246.82 Å, 4320.73 Å, and 4415.56 Å, the 3D effects were studied with the approach described above, and the estimated corrections obtained are Δ_{3D} = +0.08 dex and Δ_{3D} = +0.01 dex, using [Fe/H] = −2 and [Fe/H] = −3, respectively.

4.1.5. Iron-peak elements: V, Cr, Mn, Fe, Co, and Ni

The equivalent widths presented in Table A.1 of about 40 lines of Fe I and 5 lines of Fe II were employed in the analysis. For other elements spectrum synthesis was employed.

For the vanadium abundance derivation, we checked 6 V I and 11 V II lines, but for half of our program stars only a few lines are strong enough to be useful. Fig. 15 shows the line V II 3727.34 Å (upper panel) and V II 3732.75 Å (lower panel) for HE 2229-4153. All stars exhibit higher abundances from the V II lines than in the results from the V I lines. The average difference in the present sample is +0.23 dex. The same discrepancy was also found by Siqueira-Mello et al. (2012) for HD 140283, and by Johnson (2002), who analyzed the V abundance in 23 metal-poor stars. Johnson suggested that the cause of this discrepancy might be that hyperfine splitting and NLTE effects had been neglected in the computations.

To evaluate the 3D effects on the V abundances, the V I 4379.23 Å and V II 3951.96 Å lines were studied with hydrodynamical models, following the method already described. For V I, the results obtained are Δ_{3D} = −0.19 dex and Δ_{3D} = −0.55 dex, using [Fe/H] = −2 and [Fe/H] = −3, respectively. On the other hand, the estimated corrections for V II are Δ_{3D} = +0.04 dex and Δ_{3D} = +0.05 dex. As a general trend, the 3D effects are stronger for V I lines and make the differences in abundances obtained from neutral and ionized species bigger.

The abundance of chromium was measured using three lines: Cr I 4254.33 Å, Cr I 4274.80 Å, and Cr I 4289.72 Å. Fig. 16 shows the results for Cr I 4254.33 Å for HE 2229-4153 (upper panel), and the abundance ratios [Cr/Fe] obtained in the present work, overlapping the results of Cayrel et al. (2004) (lower panel). The lower abundance of Cr with respect to Fe observed in the metal-poor stars was also found in the present results. The decrease of [Cr/Fe] with [Fe/H] is confirmed by the present result. However, Bonifacio et al. (2009) were also able to observe a Cr II line, and have shown (see their Fig. 8) an increasing discrepancy between the Cr abundance deduced from the neutral and the ionized species when [Fe/H] decreases (see also Lai et al. 2008). As a consequence, the trend of [Cr/Fe] vs [Fe/H] is very probably due to a NLTE effect.

Five lines of Mn I were analyzed to measure the manganese abundance, and the hyperfine structure was properly taken into account (Kurucz & Bell 1995, Ivans et al. 2006). However, the Mn I 4082.94 Å line is weaker than the others and was measured only in HE 0524-2055. Moreover, three lines belong to the resonance triplet: Mn I 4030.75 Å, Mn I 4033.06 Å, and Mn I 4034.48 Å. Fig. 17 shows the line Mn I 4030.75 Å in CS 30315-029 (upper panel) as an example. It is well-known that the abundances derived from this triplet are systematically lower than the results from subordinate lines in very metal-poor giant stars. Cayrel et al. (2004) reported an average difference of 0.4 dex among the stars of the ESO LP “First Stars,” and the present results confirm their value.

We adopted the abundances of Mn deduced from the subordinate lines and not the resonance lines as the final results, because the resonance lines are more susceptible to NLTE effects (Bonifacio et al. 2009). Fig. 17 compares our results with those obtained by Cayrel et al. (2004), which also gave preference to the abundances deduced from the subordinate lines (lower panel). The underabundances of Mn with respect to Fe derived for our sample stars agree with results from the literature.

The Mn abundances obtained from the resonance triplet are also affected more strongly by the 3D modeling. Our estimated computations with hydrodynamical models applied to

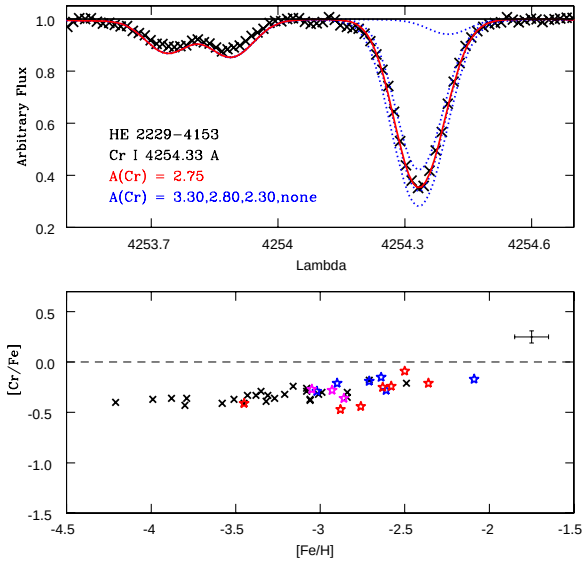

Fig. 16. Upper panel: Cr abundances from the Cr I 4254.33 Å line for HE 2229-4153. Symbols are the same as in Fig. 3. Lower panel: comparison of the abundance ratio [Cr/Fe] obtained in this work with the LTE results from Cayrel et al. (2004). Symbols are the same as in Fig. 8.

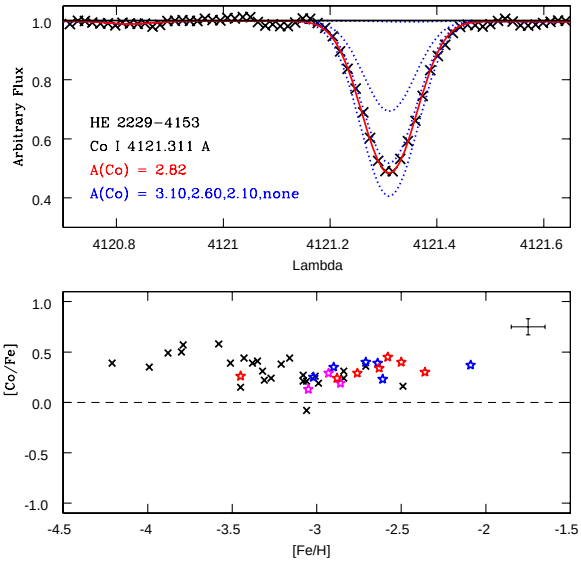

Fig. 18. Upper panel: Co abundance from the Co I 4121.31 Å line for HE 2229-4153. Symbols are the same as in Fig. 3. Lower panel: comparison of the abundance ratio [Co/Fe] obtained in this work with the LTE results from Cayrel et al. (2004). Symbols are the same as in Fig. 8.

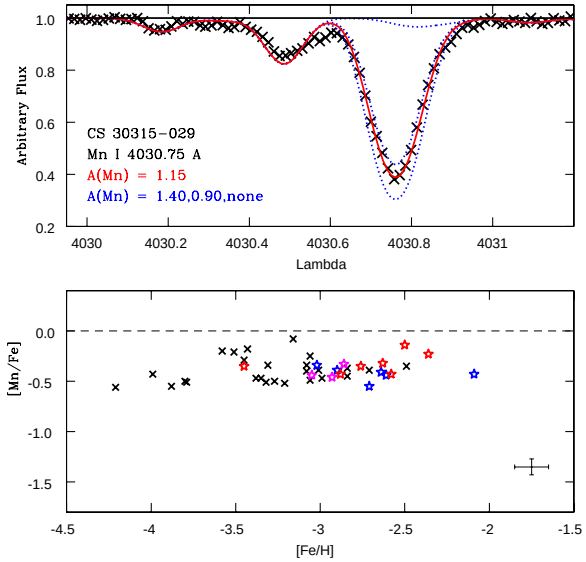

Fig. 17. Upper panel: Mn abundance from the Mn I 4030.75 Å line for CS 30315-029. Symbols are the same as in Fig. 3. Lower panel: comparison of the abundance ratio [Mn/Fe] obtained in this work with the LTE results from Cayrel et al. (2004). Symbols are the same as in Fig. 8.

Mn I 4030.75 Å, Mn I 4033.06 Å, and Mn I 4034.48 Å lines obtained the corrections $\Delta_{3D} = -0.18$ dex and $\Delta_{3D} = -0.57$ dex, with [Fe/H] = −2 and [Fe/H] = −3, respectively. The same procedure applied to the subordinate line located at 4041.35 Å results in $\Delta_{3D} = +0.02$ dex and $\Delta_{3D} = -0.18$ dex.

The same good agreement is obtained for cobalt abundances, which were derived based on four Co I lines, and Fig. 18 shows (in the upper panel) the Co I 4121.31 Å line for HE 2229-4153 as an example. The results for all the stars are compared with the abundances obtained in Cayrel et al. (2004) (lower panel); in this case there is an overabundance of Co with respect to Fe.

Nickel was the heaviest iron-peak element derived in the present work, based on 2 Ni I lines: 3807.14 Å and 3858.29 Å. Fig. 19 presents (in the upper panel) the fitting used for Ni I 3858.29 Å for CS 30315-029 as an example, and compares the results with the abundances from the ESO LP "First Stars" in the lower panel. As for other iron-peak elements, there is no apparent difference in the Ni abundances among the r-I and r-II stars (or the normal stars).

Zinc is an interesting element because it represents (together with other elements) the transition between the iron peak and the heavy elements region. However, the Zn abundance is mainly measured based on the Zn I 4722.15 Å and Zn I 4810.53 Å lines, not covered by the wavelength ranges of the present spectra.

4.2. Neutron-capture elements

The line list retained to derive the abundances of the heavy elements was established carefully, by verifying the intensity of different lines of a same element, the presence of blends, and the signal-to-noise ratio (S/N) of the observed spectra. These verifications are particularly important in the blue regions. The final line list with individual abundances is listed in Table A.2.

To organize the discussion in terms of the r-process, the trans-iron elements are grouped into the first peak (from gallium to cadmium), the second peak (from barium to tantalum), the third peak (from tungsten to bismuth), and the actinides region (thorium and uranium).

4.2.1. First-peak region elements

The strontium abundances were derived from the Sr II 4077.72 Å and Sr II 4215.52 Å lines. A third line, Sr II 4161.79 Å, was also

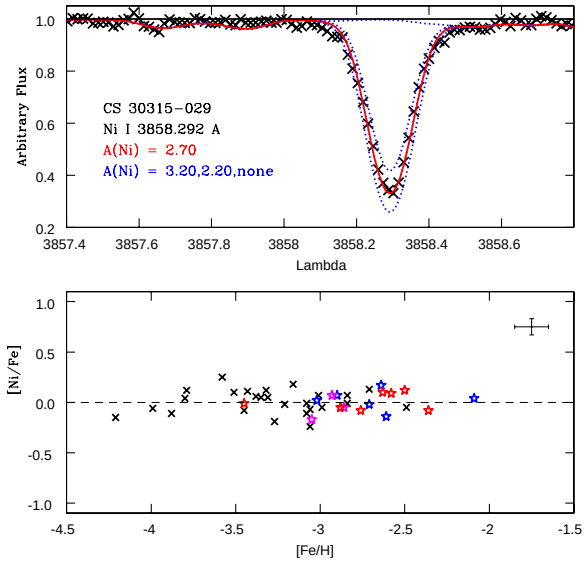

Fig. 19. Upper panel: Ni abundance from the Ni I 3858.29 Å line for CS 30315-029. Symbols are the same as in Fig. 3. Lower panel: comparison of the abundance ratio [Ni/Fe] obtained in this work with the LTE results from Cayrel et al. (2004). Symbols are the same as in Fig. 8.

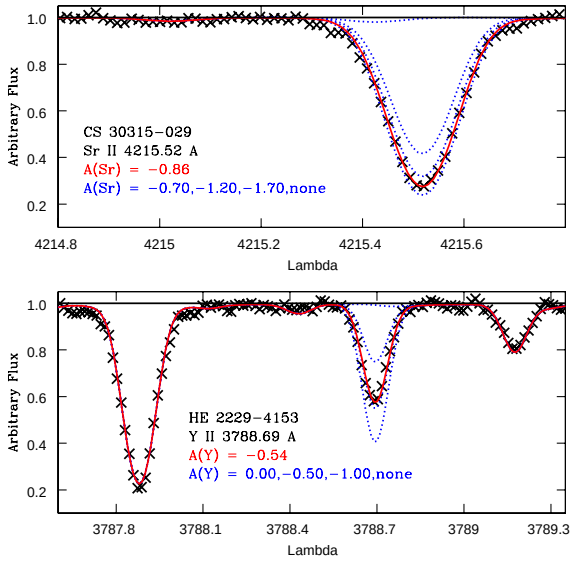

Fig. 20. Upper panel: Sr abundance from the Sr II 4215.52 Å line for CS 30351-029. Lower panel: Y abundance from the line Y II 3788.69 Å line for HE 2229-4153. Symbols are the same as in Fig. 3.

checked, but it was too weak in most stars and was excluded from the final results. Fig. 20 shows (in the upper panel) the fit of the Sr II 4215.52 Å line for CS 30351-029. Using NLTE computations, Andrievsky et al. (2011) studied the Sr abundances in the sample observed during the LP "First Stars", and they obtained the average correction $\Delta_{NLTE} = +0.09$ dex.

The yttrium abundances were obtained after checking five Y II lines: 3774.33 Å, 3788.69 Å, 3818.34 Å, 3950.35 Å, and 4398.01 Å. In some stars, one or more lines are too weak and were not used. Fig. 20 presents the result for the Y II 3788.69 Å line for HE 2229-4153. For zirconium, the abundances were derived from four Zr II lines: Zr II 3836.76 Å, Zr II 4161.21 Å, Zr II 4208.98 Å, and Zr II 4317.30 Å. Fig. 21 shows (in the upper panel) the result obtained for the Zr II 3836.76 Å for HE 2229-4153.

Fig. 22 shows the abundances ratios [Sr/Fe], [Y/Fe], and [Zr/Fe], as a function of metallicity, [Fe/H], for the present sample. These ratios are also compared with the results obtained by François et al. (2007), showing excellent agreement. It is interesting to note that the r-II stars are located around [Fe/H] ~ -3, and most of r-I stars appear at higher metallicities. The abundance ratios are stable, but the scatter seems to become important for [Fe/H] < -3 in normal stars. For the r-I and r-II stars, a remarkably consistent first-peak abundance is observed across the entire metallicity range.

The best lines to derive the molybdenum abundances are located in the ultraviolet region, but it was possible to derive upper limits for two sample stars, CS 30315-029 and HE 0524-2055, using the Mo I line located at 3864.10 Å, which is rather weak. In the case of ruthenium, the abundance was derived for three stars: CS 30315-029, HE 0057-4541, and HE 0524-2055. The Ru I lines used were 3498.94 Å, 3728.02 Å, and 3799.35 Å, which also allowed us to derive upper limits for HE 0240-0807 and HE 2229-4153. However, the difficulty in placing the continuum, as well as the blends with strong lines, indicate that the reported Ru abundances should be taken with caution.

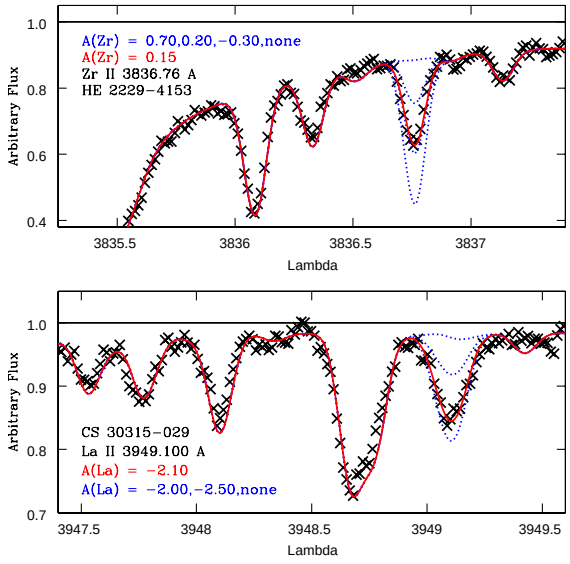

Fig. 21. Upper panel: Zr abundance from the Zr II 3836.76 Å line for HE 2229-4153. Lower panel: La abundance from the line La II 3949.10 Å line for CS 30351-029. Symbols are the same as in Fig. 3.

The same difficulty due to the weakness of the lines was found for palladium. Based on two Pd I lines, located at 3404.58 Å and 3516.94 Å, only upper limits were derived for CS 30315-029 and HE 2229-4153.

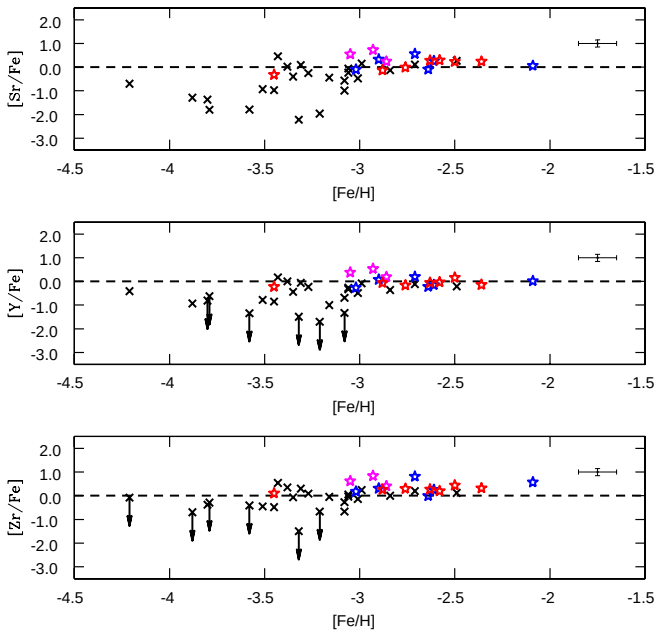

Fig. 22. [Sr, Y, Zr/Fe] vs. [Fe/H] for the present sample compared with results for metal-poor stars by François et al. (2007). Symbols are the same as in Fig. 8. Upper limits from François et al. are indicated as black arrows.

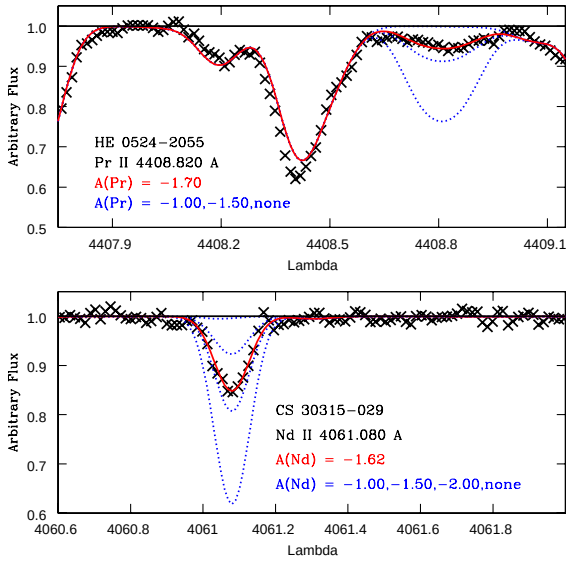

Fig. 23. Upper panel: Pr abundance from the Pr II 4408.82 Å line for HE 0524-2055. Lower panel: Nd abundance from the Nd II 4061.08 Å line for CS 30351-029. Symbols are the same as in Fig. 3.

4.2.2. Second-peak region elements

The barium abundance was derived from the Ba II 4554.02 Å line. This wavelength is not covered by our new high-resolution spectra, thus the HERES spectra were used. The exception was CS 30315-029, for which a high-resolution spectrum obtained in the framework of the LP "First Stars" – and not analyzed previously – was used. The hyperfine structure was taken into account based on McWilliam (1998). The Ba II 3891.78 Å and Ba II 4130.64 Å lines, which are in the wavelength range covered by the new data, were also checked, but they are too weak to yield reliable abundances. The barium abundances derived are similar to those reported by B05 (Table 1). Andrievsky et al. (2009) used NLTE computations to obtain the Ba abundances in the sample of the LP "First Stars," reporting an average correction of $\Delta_{NLTE} = +0.17$ dex. However, it is important to note that this correction strongly depends on the effective temperature and metallicity (see Fig. 4 in their paper).

For lanthanum abundances, we checked 14 La II lines using experimental oscillator strengths from Lawler et at. (2001a) and hyperfine structures from Ivans et al. (2006). Fig. 21 shows the fit used for the La II 3949.10 Å line for CS 30351-029 (lower panel).

Based on consideration of 15 Ce II lines, the abundance of cerium was derived for six of our program stars. For HE 0105-6141 only an upper limit was obtained. Improved laboratory transition probabilities were adopted from Lawler et al. (2009). The praseodymium abundance was derived only for CS 30315-029, HE 0240-0807, HE 0524-2055, and HE 2229-4153, after checking 11 Pr II lines. Upper limits were obtained for the other stars. New oscillator strengths were obtained from Li et al. (2007) or Ivarsson et al. (2001), and the hyperfine structures were calculated based on Sneden et al. (2009). Fig. 23 shows in the upper panel the result for the Pr II 4408.82 Å line for HE 0524-2055.

For neodymium, the abundance derivation was robust for all of our program stars, based on 16 Nd II lines, with experimental oscillator strengths from Den Hartog et al. (2003). Fig. 23 presents (in the lower panel) the Nd II 4061.08 Å line fit for CS 30351-029, as an example. The samarium abundance was derived after checking ten Sm II lines, but for HE 0516-3820 only an upper limit was obtained. Note that the odd-Z elements have lower abundances than the even-Z elements.

Europium was derived for all of our program stars, using five Eu II lines in the best cases, and the hyperfine structures for the transitions were obtained from Kurucz data base[6]. Europium presents two stable isotopes, ^{151}Eu and ^{153}Eu, and the solar system isotopic ratio of 0.48:0.52 (Arlandini et al. 1999) for Eu 151:153 was chosen for the calculation. Fig. 24 shows the results for CS 30351-029 (upper panel) and HE 0524-2055 (lower panel), using Eu II 4129.72 Å line. Mashonkina et al. (2012) present NLT corrections for Eu abundances in cool stars, but the estimated values are lower than $\Delta_{NLTE} = +0.10$ dex for our sample stars.

Fig. 25 shows the abundances ratios [Ba/Fe], [La/Fe], and [Eu/Fe], as a function of metallicity, [Fe/H], for the present sample. These ratios are also compared with the results obtained by François et al. (2007).

After checking seven Gd II lines, the gadolinium abundance was derived for six of our program stars. For HE 0105-6141, only an upper limit was obtained. Fig. 26 shows (in the upper panel) the result for the Gd II 3768.40 Å line for HE 0524-2055. The terbium abundance was derived only for CS 30315-029, and an upper limit was obtained for HE 0240-0807 and HE 0524-2055, based on three weak Tb II lines with new atomic transition probabilities from Lawler et al. (2001b), and hyperfine structure from Lawler et al. (2001c).

[6] http://kurucz.harvard.edu/atoms/6301/

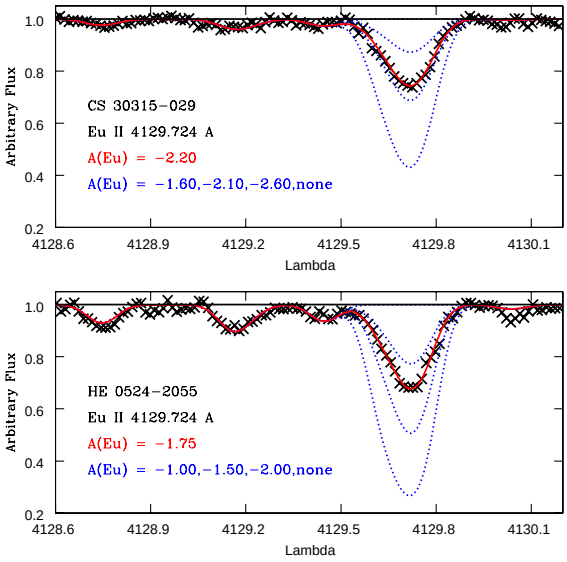

Fig. 24. Europium abundance from the line Eu II 4129.72 Å line for CS 30351-029 (upper panel) and for HE 0524-2055 (lower panel). Symbols are the same as in Fig. 3.

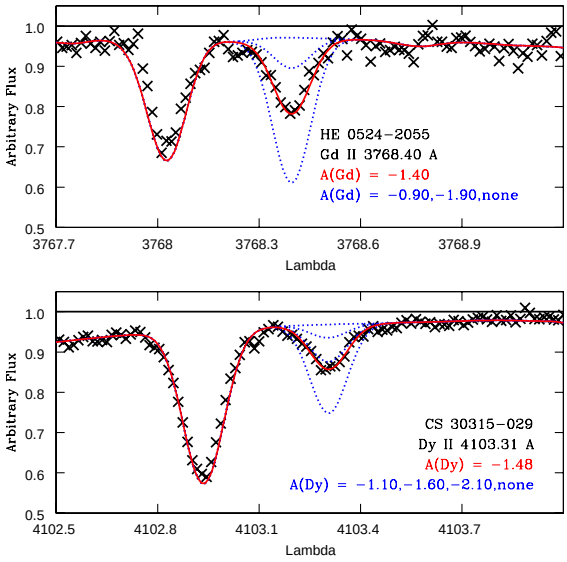

Fig. 26. Upper panel: Gd abundance from the Gd II 3768.40 Å line for HE 0524-2055. Lower panel: Dy abundance from the Dy II 4103.31 Å line for CS 30351-029. Symbols are the same as in Fig. 3.

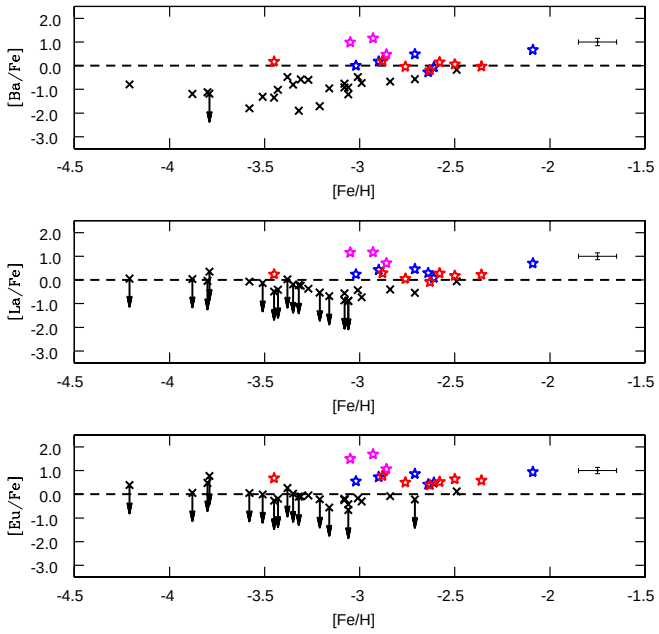

Fig. 25. [Ba, La, Eu/Fe] vs. [Fe/H] for the present sample compared with results for metal-poor stars by François et al. (2007). Symbols are the same as in Fig. 8. Upper limits from François et al. are indicated as black arrows.

The dysprosium abundance was derived from nine Dy II lines in the best case. Fig. 26 presents the Dy II 4103.31 Å line for CS 30351-029 as an example of the fitting procedure. For the holmium abundance, the Ho II 3796.74 Å and Ho II 3810.73 Å lines were checked using the hyperfine structure from Worm et al. (1990), as reported and adopted by Lawler et al. (2004), who provided log gf's for these lines. An abundance estimate was not possible to obtain for HE 0105-6141, and for HE 0516-3820 an upper limit was obtained.

We also checked five Er II lines, three Tm II lines, and one Yb II line. The erbium abundance was derived for all of our program stars except HE 0105-6141, and for HE 0516-3820 only an upper limit was obtained. A robust result for the thulium abundance was derived only for CS 30315-029, and upper limits only were obtained for HE 0057-4541, HE 0240-0807, and HE 2229-4153. From the Yb II 3694.20 Å line, the ytterbium abundance was derived for all of our program stars. The heavier elements from the second-peak region were explored, but no useful lines were found.

4.2.3. Third-peak region elements and the actinides

Upper limits on the osmium abundance were derived for CS 30315-029 and HE 0240-0807, based on the lines Os I 4260.85 Å and Os I 4420.47 Å. For the iridium abundance, the lines Ir I 3513.65 Å and Ir I 3800.12 Å were checked, and upper limits were obtained for CS 30315-029, HE 057-4541, HE 0240-0807, and HE 0524-2055.

The Th II 4019.13 Å line was used to derive the thorium abundance. A robust result was obtained for CS 30315-029, and upper limits were obtained for HE 057-4541, HE 0240-0807, and HE 0524-2055. According to Mashonkina et al. (2012), an NLTE correction of Δ_{NLTE} = +0.12 dex should be applied for the Th abundance in a star with $T_{\rm eff}$ = 4500 K, log g = 1.0 [cgs], and [Fe/H] = −3, similar with the atmospheric parameters adopted for CS 30315-029.

5. Discussion

Fig. 27 compares for each of our program stars the heavy-element abundances obtained in this work with the abundance pattern of the extremely metal-poor r-II uranium-rich star CS 31082-001, for which spectra from UVES and STIS/Hubble Space Telescope were used to derive accurate abundances (Barbuy et al. 2011; Siqueira-Mello et al. 2013). This star is

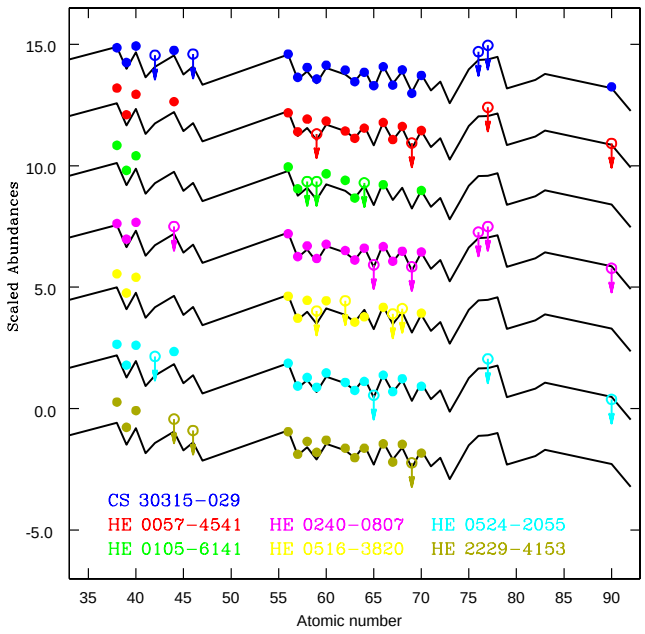

Fig. 27. Comparison of the element abundances obtained in this work with the abundance pattern of the extremely metal-poor r-II uranium-rich star CS 31082-001 (black line). An arbitrary offset was applied to distinguish the individual program stars. The error bars are smaller than the dot sizes.

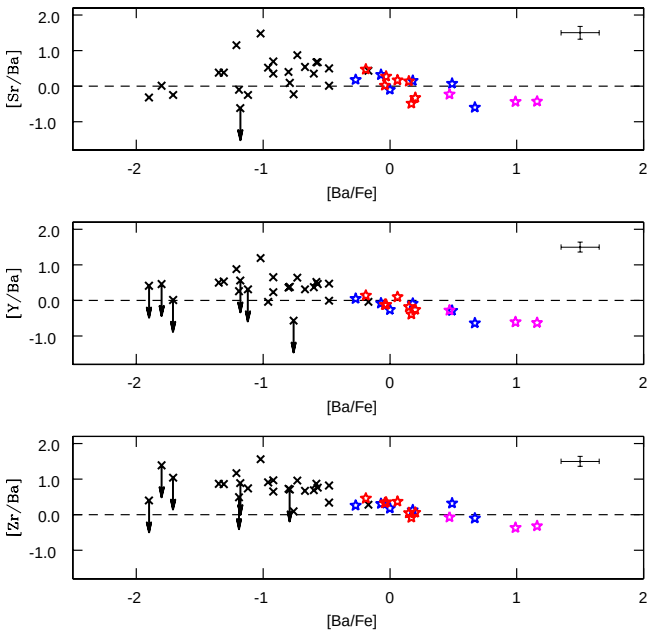

Fig. 28. [Sr, Y, Zr/Ba] as functions of [Ba/Fe] obtained in this work compared with results for metal-poor stars by François et al. (2007). Symbols are the same as in Fig. 8.

taken to be representative of r-II stars, whose abundance patterns are almost identical, except for those beyond the third-peak region (Pb and Th). The abundances for CS 31082-001 were rescaled to match the europium abundance for each r-I star, and the results were shifted vertically to aid readability. This comparison shows a remarkable agreement of the abundance pattern of the second-peak region elements, suggesting a common origin for these elements in these two classes of stars (r-I and r-II). In other words, in terms of chemical enrichment of the second-peak region neutron-capture elements, there seems to be little or no difference between r-I and r-II stars. Usually, the main r-process is invoked to explain the origin of this pattern.

By way of comparison, Fig. 27 also shows the enhancement of first peak region elements for r-I stars with respect to r-II stars. The abundance ratios [Sr/Fe], [Y/Fe], and [Zr/Fe] agree well with the data of François et al. (2007), as shown in Fig. 22, and our data confirm that the dispersion of these ratios is remarkably low for stars with [Fe/H] > -3. To evaluate the overabundance of the first-peak elements compared with the general abundance level of the main r-process, Fig. 28 shows the abundance ratios [Sr/Ba], [Y/Ba], and [Zr/Ba], as functions of [Ba/Fe]. These comparisons, already done in the literature (e.g., B05; François et al. 2007), represent the ratio [first-peak/second-peak], as a function of r-process enrichment. The [first-peak/second-peak] ratio increases as [Ba/Fe] values decreases, until ~ -1.5, thus r-I stars have intermediate values of [Sr, Y, Zr/Ba] between r-II stars and the stars without r-process enhancement (with low values of [Ba/Fe]). In addition, a break in the abundance trends may be present at the lowest [Ba/Fe] ratios. The results point toward a production of first-peak elements that is, at least in part, independent of the second-peak element production.

Among the elements from the second-peak region, the abundance ratios as a function of r-process enrichment present constant values. Fig. 29 shows the [La/Ba] and [Eu/Ba] abundance ratios, as a function of [Ba/Fe]. Setting aside upper limits, these ratios give the average values [La/Ba] = +0.16 and [Eu/Ba] = +0.51 (dotted lines in the figure). As comparison, the solar system r-process abundances, according to Simmerer

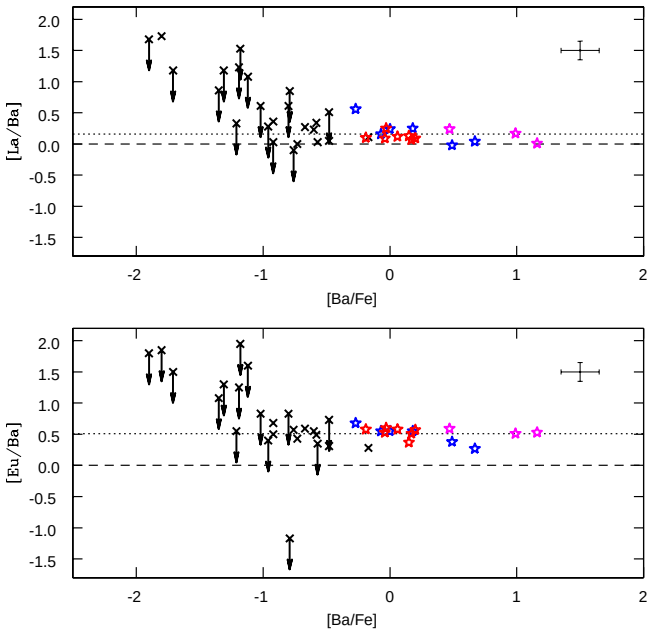

Fig. 29. [La/Ba] (upper panel) and [Eu/Ba] (lower panel) as functions of [Ba/Fe] obtained in this work compared with results for metal-poor stars by François et al. (2007). Symbols are the same as in Fig. 8. The dotted lines represent [La/Ba] = +0.16 and [Eu/Ba] = +0.51.

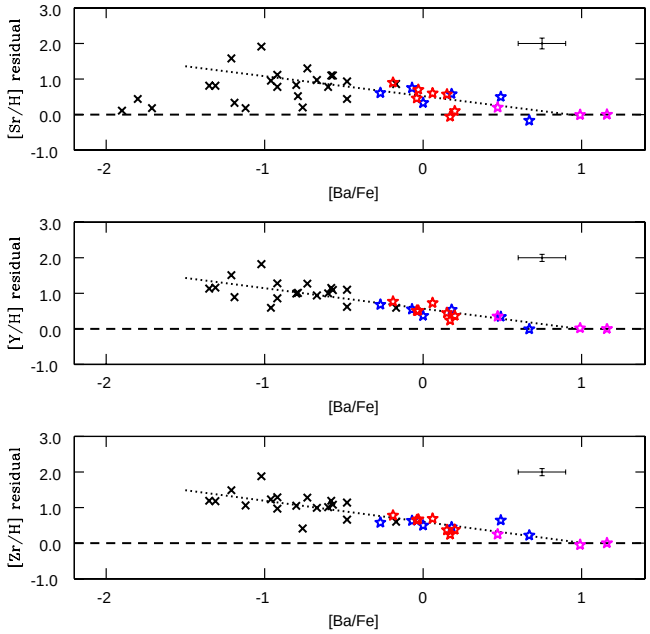

Fig. 30. Residual [Sr, Y, Zr/H] abundance ratios in comparison with the r-II star CS 31082-001 as a function of [Ba/Fe] for our program stars compared with results for metal-poor stars by François et al. (2007). Symbols are the same as in Fig. 8.

et al. (2004), give the abundance ratios $[La/Ba]_r = +0.17$ and $[Eu/Ba]_r = +0.70$. On the other hand, the abundance pattern obtained in the atmosphere of CS 31082-001, a template of main r-process (r-II) star, give the ratios $[La/Ba]_{r-II} = +0.01$ and $[Eu/Ba]_{r-II} = +0.53$. The flatness of the second-peak elemental abundances for both r-I and r-II stars, as can be seen in Fig. 29, is evidence that the main r-process similarly affects the elements in r-I and r-II stars, because the dispersion around these mean lines can account for the errors.

Indeed, the r-II stars are considered to be enriched in heavy elements by a main r-process component, and the difference observed between the abundance enhancement of first-peak elements in r-I relative to r-II stars, instead, should be due to a so-called weak component (e.g., Wanajo & Ishimaru 2006; Montes et al. 2007). We computed the residual abundances of Sr, Y, and Zr in our sample stars and in the sample from François et al. (2007), with respect to CS 31082-001, which was taken to be representative of r-II stars. Fig. 30 shows the results, and the dotted lines represent the average trend observed in the residual abundances. For [Sr/H], the stars with the lowest [Ba/Fe] values were not taken into account because of the break in the trend that might be present. The results present a continuum behavior for the enhancement in weak r-process, from the r-II stars to the normal metal-poor stars, with an intermediate value for the r-I stars, therefore showing that the classification in r-I and r-II, as established originally by Beers & Christlieb (2005), could be seen as *ad hoc*. This pattern should appear because of differences in the level of main r-process, which hide the weak r-process products with different efficiencies. The discussion suggests that the r-I stars therefore appear to exhibit a clear fraction of weak r-process in their abundance patterns, but in the r-II stars this weak component should be completely hidden.

The slopes a (and coefficients of determination R^2) of the regression lines are $a=-0.5588$ ($R^2=0.5498$), $a=-0.5730$ ($R^2=0.7382$), and $a=-0.5910$ ($R^2=0.7448$), for [Sr/H], [Y/H], and [Zr/H], respectively. These results show that the contributions from the weak r-process to the abundances of Sr, Y, and Zr are very similar. For the other first peak region elements, it was not possible to obtain a clear picture because of the low number of stars with derived abundances. Considering [Ba/Fe]~ -1.5 as the minimum limit for the presence of weak r-process, according to the break observed in [Sr/H], it is possible to estimate the maximum contribution from weak r-process expected for these elements by comparing with the pattern observed in r-II stars. This exercise gives the absolute abundances $A(Sr)_{max} = 4.28$, $A(Y)_{max} = 3.64$, and $A(Zr)_{max} = 4.07$, which should represent the maximum abundances that can be produced by the weak process in the chemical content of metal-poor stars. It is important to note that the estimates were made assuming that there is no weak r-process in stars with [Ba/Fe] < -1.5.

The classification of r-I and r-II stars used in this work is strictly based on the criteria of Beers & Christlieb (2005). The three r-II stars from the LP "First Stars" are CS 22892-052 ([Eu/Fe] = +1.49, [Ba/Eu] = −0.48), CS 22953-003 ([Eu/Fe] = +1.05, [Ba/Eu] = −0.56), and CS 31082-001 ([Eu/Fe] = +1.69, [Ba/Eu] = −0.53). However, as shown in Fig. 28, the ratios [first-peak/second-peak] exhibit the lowest values in CS 22892-052 and CS 31082-001, which can be assumed as the ratio that arises only from the main r-process, whereas CS 22953-003 appears to exhibit an excess of first-peak elements, typical of r-I stars. If [first-peak/second-peak] ratio could be used as an additional criterion to classify stars in r-I or r-II, CS 22953-003 should be re-classified as an r-I star. On the other hand, the reverse is also true: BD+17:3248 (François et al. 2007) is an r-I star ([Eu/Fe] = +0.93, [Ba/Eu] = −0.24) showing no evidences of weak r-process component in the abundance pattern (see Fig. 28 and Fig. 30), and should be re-classified as an r-II star with the additional criterion. It is important to note that the cases of borderline stars can be now discussed owing to the good quality of the data. In this sense, it is possible to find a real difference between the two groups of stars: the fraction of weak r-process is not relevant in the abundance pattern of r-II stars, but becomes evident in r-I stars. In other words, r-I and r-II stars are now confirmed to indicate different chemical enrichment histories.

Fig. 31 shows the residual abundances in the sample stars with respect to an average pattern based on the abundances of CS 31082-001 and CS 22892-052 (upper panel), as well as an average of the results (lower panel). The dashed lines represent the null value to indicate the agreement between the abundance level in the r-I stars and in the r-II star. The abundance pattern shown in the lower panel of Fig. 31 should represent the products from this incomplete r-process mechanism, and from the present results, a contribution to the abundances of some second-peak region elements from the weak r-process may be also present.

As a general conclusion, we suggest that to understand the nucleosynthesis of the r-elements, it is important to study r-I and r-II stars together.

5.1. Radioactive chronometry for CS 30315-029

CS 30315-029 is the only star in the sample in which Th was detected. In Hill et al. (2002) and Barbuy et al. (2011), the r-II star CS 31082-001 was shown to present an actinide boost disturbing the radioactive chronometers, with the consequence that chronometer indicators between a radioactive element and Eu would result in negative ages. The U/Th ratio appears to be the most reliable chronometer in such cases. Fig. 27 shows that the

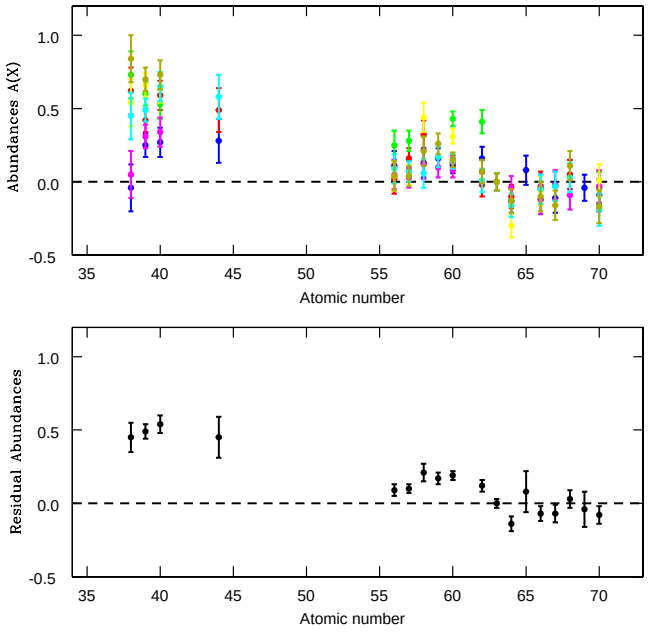

Fig. 31. Upper panel: the residual abundances with respect to an average pattern based on the abundances of CS 31082-001 and CS 22892-052 in the present sample. Lower panel: the average residual abundance. Symbols are the same as in Fig. 27.

thorium abundance in the r-I star CS 30315-029 seems to be at the same level relative to the second r-process peak elements as the one observed for CS 31082-001, which indicates the likely presence of an actinide boost. Indeed, for CS 31082-001 we obtain log(Th/Eu) = −0.26 ± 0.14 and for CS 30315-029 this value is log(Th/Eu) = −0.21 ± 0.16.

In the present sample, U II lines were not measurable, excluding the ratio U/Th as a possible age indicator. Therefore, we applied age derivation using the radioactive element Th alone. The ages can be derived from the ratios, as given for example in Cayrel et al. (2001):

$$\Delta t(\mathrm{Gyr}) = 46.7[\log(\mathrm{Th/r})_{\mathrm{init}} - \log(\mathrm{Th/r})_{\mathrm{now}}].$$

We checked several production ratios (PR) from theoretical work. These consist of the initial abundance ratios (zero-decay) expected to have occurred in the early Galaxy, obtained from r-process models, which are compared with the currently derived abundances. All the results are obtained from site-independent models or those involving high-entropy neutrino-driven winds of neutron-rich matter in core-collapse supernova, the classic astrophysical site of the main r-process. It is important to note that the chronometric ages are found to be relatively insensitive to astrophysical modeling (if reasonable parameters are chosen; Wanajo et al. 2002, 2003), but are sensitive to the nuclear data adopted (Goriely et al. 2001; Schatz et al. 2002). From Cowan et al. (1999), we used their best result for Th/Eu based on the extended Thomas-Fermi model with quenched shell effects far from stability ETFSI-Q (least-squares). The same model was used by Cowan et al. (2002) for Th/Ir, but an average value based on the ETFSI-Q, ETFSI-Q (least-squares) and finite-range droplet model with microscopic shell corrections (FRDM+HFB) was adopted for Th/Eu in this case. Schatz et al. (2002) have conducted an investigation of the influence of β-decay rates, mass models, fission processes, and model uncertainties on the age determination, presenting their best predictions of the zero-age abundance for several ratios. Different initial electron fractions (Y_e) were used by Wanajo et al. (2002) to derive the consistent age of CS 31082-001 for Th/Eu and U/Th, and we used the results for Th/Eu obtained with Y_e = 0.40. Wanajo (2007) used a similar model, but adopting hot and cold r-process conditions (see details in his paper). From Kratz et al. (2007), we adopted the Th results based on their new r-process calculations using Fe-peak seeds, which yield the best overall fit to the stable abundance data for masses $A > 125$, with the present-day observed solar system elemental abundances for the stable elements.

The ages derived are very sensitive to the adopted production ratios. In general, the radioactive chronometers involving second-peak region stable elements give ages that are too young, or even negative ages, stressing the occurrence of an actinide boost in CS 30315-029. Table 8 presents the results, and the best values (in boldface) were selected based on the ages obtained for CS 31082-001. Hill et al. (2002) reported an age of 14.0 ± 2.4 Gyr for CS 31082-001. The radioactive pairs used for CS 30315-029 are those that give results for CS 31082-001 consistent with the age from Hill et al. (2002). Only the production ratios from Wanajo et al. (2002) and Wanajo (2007) give reasonable ages, as a result of their models adjusted to the abundance pattern of CS 31082-001. The average age from the best production ratios in Table 8 obtained for CS 30315-029 is 13.5 ± 3.4 Gyr, with the standard deviation of the values taken as the uncertainty.

Table 8. Computed production ratios (PR) of Th vs.some stable *r*-process elements, observed abundance ratios, and age estimates.

Chrono.	log (PR)	Ref.	CS 31082-001	Age	CS 30315-029	Age
Pair			log (Th/X)	(Gyr)	log (Th/X)	(Gyr)
Th/La	−0.60	S02	−0.36	−11.21	−0.39	−10.01
	−0.01	**W07a**	**−0.36**	**+16.35**	**−0.39**	**+17.55**
	+0.12	W07b	−0.36	+22.42	−0.39	+23.62
Th/Ce	−0.79	S02	−0.69	−4.67	−0.80	+0.25
	+0.06	W07a	−0.69	+35.03	−0.80	+39.94
	−0.25	W07b	−0.69	+20.55	−0.80	+25.47
Th/Pr	−0.30	S02	−0.19	−5.14	−0.32	+1.03
	+0.60	W07a	−0.19	+36.89	−0.32	+43.06
	+0.25	W07b	−0.19	+20.55	−0.32	+26.71
Th/Nd	−0.91	S02	−0.83	−3.74	−0.89	−0.86
	−0.26	W07a	−0.83	+26.62	−0.89	+29.50
	−0.68	W07b	−0.83	+7.01	−0.89	+9.88
Th/Sm	−0.61	S02	−0.56	−1.87	−0.69	+4.20
	+0.01	W07a	−0.56	+26.62	−0.69	+32.69
	−0.27	**W07b**	**−0.56**	**+13.54**	**−0.69**	**+19.61**
Th/Eu	−0.32	C99	−0.26	−2.80	−0.21	−5.32
	−0.29	C02	−0.26	−1.40	−0.21	−3.92
	−0.33	S02	−0.26	−3.27	−0.21	−5.79
	+0.05	**W02**	**−0.26**	**+14.48**	**−0.21**	**+11.96**
	−0.37	K07	−0.26	−5.14	−0.21	−7.66
	+0.49	W07a	−0.26	+35.03	−0.21	+32.50
	+0.07	**W07b**	**−0.26**	**+15.41**	**−0.21**	**+12.89**
Th/Gd	−0.81	S02	−0.77	−1.87	−0.60	−9.81
	+0.42	W07a	−0.77	+55.57	−0.60	+47.63
	−0.37	**W07b**	**−0.77**	**+18.68**	**−0.60**	**+10.74**
Th/Tb	−0.12	S02	+0.03	−7.01	−0.05	−3.27
	+0.73	W07a	+0.03	+32.69	−0.05	+36.43
	+0.48	W07b	+0.03	+21.02	−0.05	+24.75
Th/Dy	−0.89	S02	−0.91	+0.93	−0.83	−2.80
	−0.07	W07a	−0.91	+39.23	−0.83	+35.49
	−0.13	W07b	−0.91	+36.43	−0.83	+32.69
Th/Er	−0.68	S02	−0.68	0.00	−0.70	+0.93
	−0.02	W07a	−0.68	+30.82	−0.70	+31.76
	−0.28	W07b	−0.68	+18.68	−0.70	+19.61
Th/Tm	+0.12	S02	+0.17	−2.34	+0.27	−6.77
	+0.65	W07a	+0.17	+22.42	+0.27	+17.98
	+0.44	**W07b**	**+0.17**	**+12.61**	**+0.27**	**+8.17**

References. S02: Schatz et al. (2002); W07: Wanajo (2007), (a) hot and (b) cold model; C99: Cowan et al. (1999); C02: Cowan et al. (2002); W02: Wanajo et al. (2002), with initial electron fraction Y_e = 0.40; K07: Kratz et al. (2007).

6. Conclusions

We analyzed seven r-I stars and derived the chemical abundances based on high-quality, high-resolution spectra.

The results obtained for the lighter element Li show that the stars have undergone the first dredge-up, and for the objects with no Li detectable an extra-mixing event may have occurred. The C abundances obtained confirm that the sample is not carbon-enhanced, per our original selection criterion. For nitrogen, the abundances were derived from the CN and NH lines, and the present values confirm the discrepancy found in the literature between these two abundance indicators.

For the α-elements Mg, Si, S, Ca, and Ti, the odd-Z elements Al, K, and Sc, and the iron-peak elements V, Cr, Mn, Fe, Co, and Ni, the results obtained in our present sample agree excellently with the values from the literature. There are no differences in the chemical content between r-I and r-II stars (or even the normal stars), in terms of these elements. Hydrodynamics models were also computed for some elements to explore the 3D corrections.

The same excellent agreement is obtained among the abundance patterns of the second-peak region elements Ba, La, Ce, Pr, Nd, Sm, Eu, Gd, Tb, Dy, Ho, Er, Tm, and Yb. The results of the r-I stars analyzed reproduce the pattern observed in the r-II star CS 31082-001. The origin of this region is associated with the main r-process, which must operate in the same way to build the chemical content observed in the atmospheres of r-I and r-II stars. The upper limits derived for the abundances of the third-peak elements also agree with the expected values from the r-II abundance pattern.

On the other hand, the derived abundances for the first peak region elements Sr, Y, Zr, Mo, Ru, and Pd, some of them as upper limits only, are enhanced with respect to the level observed in the r-II stars. In addition, this overabundance is higher in stars with lower [Ba/Fe] ratios. In other words, the abundance level obtained in r-I stars is between the lowest value derived in r-II stars and the highest one observed in the normal stars. It is important to note that the behavior of [first-peak/Fe] ratios as a function of metallicity [Fe/H] seems to be the same among all the stars (r-I, r-II, and normal stars). Indeed, a constant ratio appears for [Fe/H] > -3, which is the metallicity region of the r-process-element enriched stars, indicating a co-production of iron and the first-peak elements. A weak r-process is claimed to explain the origin of these elements, and several models are available in the literature (e.g., Montes et al. 2007; Wanajo 2013). The comparison between the calculated patterns and the observational evidence can perhaps shed some light on this problem.

The thorium abundance derived in CS 30315-029 shows that an actinide boost most likely exists for this star, which currently is the most metal-deficient object with r-process enhancement. Several r-process models were applied to calculate the age of the star based on radioactive chronometry, but the lack of uranium abundance in CS 30315-029 does not permit us to use the ratio U/Th, the only robust radioactive pair in stars with actinide boost.

Acknowledgements. CS and BB acknowledge grants from CAPES, CNPq and FAPESP. MS and FS acknowledge the support of CNRS (PNCG and PNPS). TCB and HS acknowledge support from grant PHY 08-22648: Physics Frontiers Center/Joint Institute for Nuclear Astrophysics (JINA), awarded by the U.S. National Science Foundation. HS acknowledges support from NSF grant PHY1102511. EC is grateful to the FONDATION MERAC for funding her fellowship. SW acknowledges support from the JSPS Grants-in-Aid for Scientific Research (23224004). This work has made use of the ADS Service (SAO/NASA), the SIMBAD database (Centre de données de Strasbourg), and of the arXiv Server (Cornell University).

References

Alonso, A., Arribas, S., Martinez-Roger, C. 1998, A&AS, 131, 209
Alonso, A., Arribas, S., Martínez-Roger, C. 1999, A&AS, 140, 261
Alvarez, R., Plez, B. 1998, A&A, 330, 1109
Andrievsky, S. M., Spite, M., Korotin, S. A., Spite, F., Bonifacio, P., Cayrel, R., Hill, V., François, P. 2008, A&A, 481, 481
Andrievsky, S. M., Spite, M., Korotin, S. A., Spite, F., François, P., Bonifacio, P., Cayrel, R., Hill, V. 2009, A&A, 494, 1083
Andrievsky, S. M., Spite, M., Korotin, S. A., Spite, F., Bonifacio, P., Cayrel, R., François, P., Hill, V. 2010, 509, 88
Andrievsky, S. M., Spite, F., Korotin, S. A., François, P., Spite, M., Bonifacio, P., Cayrel, R., Hill, V. 2011, A&A, 530, 105
Anstee, S. D., O'Mara, B. J. 1995, MNRAS, 276, 859
Aoki, W., Beers, T. C., Christlieb, N., Norris, J. E., Ryan, S. G., Tsangarides, S. 2007, ApJ, 655, 492
Arlandini, C., Käppeler, F., Wisshak, K., Gallino, R., Lugaro, M., Busso, M., Straniero, O. 1999, ApJ, 525, 886
Barbuy, B., Spite, M., Hill, V., Primas, F., Plez, B., Cayrel, R., Spite, F., Wanajo, S., Siqueira-Mello, C., Andersen, J., Nordström, B., Beers, T. C., Bonifacio, P., François, P., Molaro, P. 2011, A&A, 534, 60
Barklem, P. S., O'Mara, B. J. 1997, MNRAS, 290, 102
Barklem, P. S., O'Mara, B. J., Ross, J. E. 1998, MNRAS, 296, 1057
Barklem, P. S., Christlieb, N., Beers, T. C., Hill, V., Bessell, M. S., Holmberg, J., Marsteller, B., Rossi, S., Zickgraf, F.-J., Reimers, D. 2005, A&A, 439, 129 (B05)
Baumueller, D., Gehren, T. 1997, A&A, 325, 1088
Beers, T. C. & Christlieb, N. 2005, ARA&A, 43, 531
Beers, T. C., Flynn, C., Rossi, S. et al. 2007, ApJS, 168, 128
Bessell, M. S. 1979, PASP, 91, 589
Bonifacio, P., Spite, M., Cayrel, R., Hill, V., Spite, F., François, P., Plez, B., Ludwig, H. -G., Caffau, E., Molaro, P., Depagne, E., Andersen, J., Barbuy, B., Beers, T. C., Nordström, B., Primas, F. 2009, A&A, 501, 519
Caffau, E., Ludwig, H.-G., Steffen, M., Freytag, B., Bonifacio, P. 2011, SoPh, 268, 255
Carpenter, J. M. 2001, 121, 2851
Cayrel, R., Hill, V., Beers, T. C., Barbuy, B., Spite, M., Spite, F., Plez, B., Andersen, J., Bonifacio, P., François, P., Molaro, P., Nordström, B., Primas, F. 2001, Nature, 409, 691
Cayrel, R., Depagne, E., Spite, M., Hill, V., Spite, F., François, P., Plez, B., Beers, T., Primas, F., Andersen, J., Barbuy, B., Bonifacio, P., Molaro, P., Nordström, B. 2004, A&A, 416, 1117
Charbonneau, P. 1995, ApJS, 101, 309
Chen, H. -C., Lallement, R., Babusiaux, C., Puspitarini, L., Bonifacio, P., Hill, V. 2013, A&A, 550, 62
Christlieb, N., Beers, T. C., Barklem, P. S., Bessell, M., Hill, V., Holmberg, J., Korn, A. J., Marsteller, B., Mashonkina, L., Qian, Y.-Z., Rossi, S., Wasserburg, G. J., Zickgraf, F.-J., Kratz, K.-L., Nordström, B., Pfeiffer, B., Rhee, J., Ryan, S. G. 2004, A&A, 428, 1027
Clough, S. A., Shephard, M. W., Mlawer, E. J., Delamere, J. S., Iacono, M. J., Cady-Pereira, K., Boukabara, S., Brown, P. D. 2005, JQSRT, 91, 233
Cowan, J. J., Pfeiffer, B., Kratz, K. -L., Thielemann, F. -K., Sneden, C., Burles, S., Tytler, D., Beers, T. C. 1999, ApJ, 521, 194
Cowan, J. J., Sneden, C., Burles, S., Ivans, I. I., Beers, T. C., Truran, J. W., Lawler, J. E., Primas, F., Fuller, G. M., Pfeiffer, B., Kratz, K. -L. 2002, ApJ, 572, 861
Dean, J. F., Warren, P. R., Cousins, A. W. J. 1978, MNRAS, 183, 569
Den Hartog, E. A., Lawler, J. E., Sneden, C., Cowan, J. J. 2003, ApJS, 148, 543
Fernie, J. D. 1983, PASP, 95, 782
François, P., Depagne, E., Hill, V. et al. 2003, A&A, 403, 1105
François, P., Depagne, E., Hill, V., Spite, M., Spite, F., Plez, B., Beers, T. C., Andersen, J., James, G., Barbuy, B., Cayrel, R., Bonifacio, P., Molaro, P., Nordström, B., Primas, F. 2007, A&A, 476, 935
Freytag, B., Steffen, M., Dorch, B. 2002, Astron. Nachr., 323, 213
Freytag, B., Steffen, M., Ludwig, H.-G., Wedemeyer-Böhm, S., Schaffenberger, W., Steiner, O. 2012, JCoPh, 231, 919
Goriely, S. & Arnould, M. 2001, A&A, 379, 1113
Goriely, S., Bauswein, A., Janka, H.-T. 2011, ApJ, 738, L32
Gustafsson, B., Edvardsson, B., Eriksson, K., Mizuno-Wiedner, M., Jørgensen, U. G., Plez, B. 2003 in Stellar Atmosphere Modeling, eds. I. Hubeny D. Mihalas K., Werner ASP Conf. Series 288 331
Gustafsson, B., Edvardsson, B., Eriksson, K., Jørgensen, U. G., Nordlund, Å., Plez, B. 2008, A&A, 486, 951
Gustafsson, B. 2009, Proceedings of the International Astronomical Union, 5, S265, pp 187-196
Hill, V., Plez, B., Cayrel, R., Beers, T. C., Nordström, B., Andersen, J., Spite, M., Spite, F., Barbuy, B., Bonifacio, P., Depagne, E., François, P., Primas, F. 2002, A&A, 387, 560

Ivanova, D. V., Shimanskii, V. V. 2000, ARep, 44, 376
Ivans, I. I., Simmerer, J., Sneden, C., Lawler, J. E., Cowan, J. J., Gallino, R., Bisterzo, S. 2006, ApJ, 645, 613
Ivarsson, S., Litzén, U., Wahlgren, G. M. 2001, PhyS, 64, 455
Johnson, J. A. 2002, ApJS, 139, 219
Kratz, K.-L., Farouqi, K., Pfeiffer, B., Truran, J. W., Sneden, C., Cowan, J. J. 2007, ApJ, 662, 39
Kupka, F., Piskunov, N., Ryabchikova, T. et al. 1999, A&AS, 138, 119
Lai, D. K., Bolte, M., Johnson, J. A., Lucatello, S., Heger, A., Woosley, S. E. 2008, ApJ, 681, 1524
Langanke, K., Thielemann F.-K., 2013, ENews 44/3, 24
Lawler, J. E., Bonvallet, G., Sneden, C. 2001a, ApJ, 556, 452
Lawler, J. E., Wickliffe, M. E., Cowley, C. R., Sneden, C. 2001b, ApJS, 137, 341
Lawler, J. E., Wyart, J.-F., Blaise, J. 2001c, ApJS, 137, 351
Lawler, J. E., Sneden, C., Cowan, J. J. 2004, ApJ, 604, 850
Lawler, J. E., Sneden, C., Cowan, J. J., Ivans, I. I., Den Hartog, E. A. 2009, ApJS, 182, 51
Li, R., Chatelain, R., Holt, R. A., Rehse, S. J., Rosner, S. D., Scholl, T. J. 2007, PhyS, 76, 577
Lind, K., Asplund, M., Barklem, P. S. 2009, A&A, 503, 541
Mashonkina, L., Ryabtsev, A., Frebel, A. 2012, A&A, 540, 98
McWilliam, A. 1998, AJ, 115, 1640
Montes, F., Beers, T. C., Cowan, J., Elliot, T., Farouqi, K., Gallino, R., Heil, M., Kratz, K.-L., Pfeiffer, B., Pignatari, M., Schatz, H. 2007, ApJ, 671, 1685
Norris, J. E., Ryan, S. G., Beers, T. C. 2001, ApJ, 561, 1034
Rieke, G. H., Lebofsky, M. J. 1985, ApJ, 288, 618
Roederer, I. U., Cowan, J. J., Karakas, A. I., Kratz, K. -L., Lugaro, M., Simmerer, J., Farouqi, K., Sneden, C. 2010, ApJ, 724, 975
Rosswog, S., Korobkin, O., Arcones, A., Thielemann, F.-K. 2014, MNRAS, in press; arXiv:1307.2939
Rothman, L. S., Gordon, I. E., Barbe, A., Benner, D. Chris, Bernath, P. F. et al. 2009, JQSRT, 110, 533
Schatz, H., Toenjes, R., Pfeiffer, B., Beers, T. C., Cowan, J. J., Hill, V., Kratz, K. -L. 2002, ApJ, 579, 626
Schlegel, D. J., Finkbeiner, D. P., Davis, M. 1998, ApJ, 500, 525
Siqueira-Mello, C., Barbuy, B., Spite, M., Spite, F. 2012, A&A, 548, A42
Siqueira-Mello, C., Spite, M., Barbuy, B., Spite, F., Caffau, E., Hill, V., Wanajo, S., Primas, F., Plez, B., Cayrel, R., Andersen, J., Nordström, B., Sneden, C., Beers, T. C., Bonifacio, P., François, P., Molaro, P. 2013, A&A, 550, 122
Simmerer, J., Sneden, C., Cowan, J. J., Collier, J., Woolf, V. M., Lawler, J. E. 2004, ApJ, 617, 1091
Sneden, C., McWilliam, A., Preston, G. W., Cowan, J. J., Burris, D. L., Armosky, B. J. 1996, ApJ, 467, 819
Sneden, C., Cowan, J. J., Ivans, I. I., Fuller, G. M., Burles, S., Beers, T. C., Lawler, J. E. 2000, ApJ, 533, 139
Sneden, C., Lawler, J. E., Cowan, J. J., Ivans, I. I., Den Hartog, E. A. 2009, ApJS, 182, 80
Spite, M., Cayrel, R., Plez, B., Hill, V., Spite, F., Depagne, E., François, P., Bonifacio, P., Barbuy, B., Beers, T., Andersen, J., Molaro, P., Nordström, B., Primas, F. 2005, A&A, 430, 655
Spite, M., Caffau, E., Andrievsky, S. M., Korotin, S. A., Depagne, E., Spite, F., Bonifacio, P., Ludwig, H. -G., Cayrel, R., François, P., Hill, V., Plez, B., Andersen, J., Barbuy, B., Beers, T. C., Molaro, P., Nordström, B., Primas, F. 2011, A&A, 528, 9
Spite, M., Andrievsky, S. M., Spite, F., Caffau, E., Korotin, S. A., Bonifacio, P., Ludwig, H.-G., François, P., Cayrel, R. 2012, A&A, 541, 143
Skrutskie, M. F., Cutri, R. M., Stiening, R. et al. 2006, AJ, 131, 1163
Takeda, Y., Kaneko, H., Matsumoto, N., Oshino, S., Ito, H., Shibuya, T. 2009, PASJ, 61, 563
Truran, J. W. 1981, A&A, 97, 391
Wanajo, S., Itoh, N., Ishimaru, Y., Nozawa, S., Beers, T. C. 2002, ApJ, 577, 853
Wanajo, S., Tamamura, M., Itoh, N., Nomoto, K., Ishimaru, Y., Beers, T. C., Nozawa, S. 2003, ApJ, 593, 968
Wanajo, S. & Ishimaru, Y. 2006, NuPhA, 777, 676
Wanajo, S. 2007, ApJ, 666, 77
Wanajo, S. 2013, ApJL, 770, L22
Wanajo, S., Sekiguchi, Y., Nishimura, N., Kiuchi, K., Kyutoku, K., Shibata, M. 2014, ApJL, submitted; arXiv:1402.7317
Winteler, C., Käppeli, R., Perego, A., Arcones, A., Vasset, N., Nishimura, N., Liebendörfer, M., Thielemann, F.-K. 2012, ApJL, 750, L22
Worm, T., Shi, P., Poulsen, O. 1990, Phys. Scr., 42, 569

Appendix A: Line lists

Table A.1. Equivalent widths (EW) measured and used to derive new atmospheric parameters and abundances of titanium and iron.

Species	λ(Å)	χ_{ex}(eV)	log gf	EW(mÅ) CS 30315-029	EW(mÅ) HE 0057-4541	EW(mÅ) HE 0105-6141	EW(mÅ) HE 0240-0807	EW(mÅ) HE 0516-3820	EW(mÅ) HE 0524-2055	EW(mÅ) HE 2229-4153
Ti I	3729.807	0.000	−0.351	33.87	58.40	45.56	60.48	40.79	65.04	——
Ti I	3741.059	0.021	−0.213	36.33	60.51	42.88	55.30	42.77	60.52	——
Ti I	3752.859	0.048	−0.019	45.86	56.77	49.56	63.77	51.83	64.67	47.54
Ti I	3924.527	0.021	−0.937	15.83	31.36	18.35	34.07	15.00	34.23	19.56
Ti I	3929.874	0.000	−1.060	——	——	——	——	——	——	10.79
Ti I	3962.851	0.000	−1.167	——	——	12.34	——	——	23.86	10.78
Ti I	3964.269	0.021	−1.184	——	——	——	——	——	——	8.79
Ti I	3998.636	0.048	−0.056	44.95	——	53.57	68.53	53.37	71.27	55.75
Ti I	4112.709	0.048	−1.758	——	7.68	——	——	——	8.58	——
Ti I	4287.403	0.836	−0.442	5.56	——	13.14	15.12	——	21.39	——
Ti I	4453.312	1.430	−0.051	——	9.81	——	11.50	4.69	9.14	6.30
Ti I	4512.734	0.836	−0.480	6.30	15.00	9.10	15.66	6.28	14.18	8.68
Ti I	4518.022	0.826	−0.325	9.20	——	——	14.47	——	——	11.79
Ti II	3913.461	1.116	−0.420	——	——	94.70	——	91.38	——	95.43
Ti II	4012.383	0.574	−1.840	87.96	91.13	73.63	——	72.16	——	73.64
Ti II	4028.338	1.892	−0.960	30.45	59.99	34.18	56.68	33.69	59.15	38.31
Ti II	4290.215	1.165	−0.850	85.88	——	78.65	——	82.98	——	85.41
Ti II	4337.914	1.080	−0.960	84.48	——	69.47	97.88	66.18	——	73.88
Ti II	4394.051	1.221	−1.780	39.89	56.80	41.36	63.31	36.88	67.32	43.75
Ti II	4395.031	1.084	−0.540	——	——	97.48	——	——	——	——
Ti II	4399.765	1.237	−1.190	66.24	89.52	66.97	93.41	62.66	96.36	73.96
Ti II	4417.714	1.165	−1.190	75.73	81.96	66.35	97.18	65.75	97.47	70.73
Ti II	4418.330	1.237	−1.970	29.46	42.92	23.50	47.88	20.14	53.55	28.64
Ti II	4443.794	1.080	−0.720	98.70	——	88.00	——	84.90	——	90.03
Ti II	4444.555	1.116	−2.240	24.56	38.28	22.34	48.98	16.78	50.11	23.55
Ti II	4450.482	1.084	−1.520	62.47	72.85	56.72	91.99	53.17	89.45	59.69
Ti II	4464.449	1.161	−1.810	43.61	54.46	37.22	68.11	34.86	70.86	40.69
Ti II	4468.507	1.131	−0.600	——	——	90.22	——	88.35	——	94.99
Ti II	4470.853	1.165	−2.020	27.84	35.31	19.01	44.12	18.75	52.32	25.58
Ti II	4501.270	1.116	−0.770	95.46	99.82	90.15	——	84.53	——	86.46
Fe I	3753.611	2.176	−0.890	55.33	82.77	58.07	83.46	59.91	87.73	59.34
Fe I	3765.539	3.237	0.482	50.72	82.44	63.82	74.11	67.17	83.57	62.68
Fe I	3805.342	3.301	0.312	46.07	67.63	63.82	75.49	56.50	71.32	59.57
Fe I	3997.392	2.727	−0.479	43.99	71.10	59.48	68.81	59.59	73.63	57.97
Fe I	4005.242	1.557	−0.610	——	——	93.89	——	——	——	——
Fe I	4021.866	2.758	−0.729	——	61.16	40.77	58.43	50.06	59.52	44.45
Fe I	4032.627	1.485	−2.377	26.88	44.21	29.80	49.88	27.55	52.40	30.93
Fe I	4062.441	2.845	−0.862	19.18	46.89	30.52	38.17	37.01	44.81	31.38
Fe I	4067.978	3.211	−0.472	16.44	47.51	36.75	42.40	38.83	45.99	34.37
Fe I	4076.629	3.211	−0.529	——	——	——	——	37.71	——	——
Fe I	4107.488	2.831	−0.879	25.17	56.41	37.87	53.20	40.81	57.86	42.82
Fe I	4114.445	2.831	−1.303	11.34	33.14	16.63	24.37	18.95	29.26	18.74
Fe I	4134.677	2.831	−0.649	31.73	61.35	44.41	57.66	49.15	63.34	47.63
Fe I	4136.998	3.415	−0.453	8.98	35.31	19.09	24.41	23.61	29.33	21.59
Fe I	4147.669	1.485	−2.104	50.25	68.46	45.53	78.33	53.53	76.80	53.24
Fe I	4153.900	3.396	−0.321	17.01	48.52	31.17	38.80	36.73	50.09	32.78
Fe I	4154.499	2.831	−0.688	25.71	——	43.63	49.27	49.67	59.04	45.02
Fe I	4154.805	3.368	−0.400	15.83	45.51	29.84	34.83	38.42	45.38	33.43
Fe I	4156.799	2.831	−0.809	24.92	58.68	44.02	51.50	42.34	61.72	44.39
Fe I	4157.780	3.417	−0.403	12.87	44.75	30.18	33.58	32.48	38.88	31.79
Fe I	4175.636	2.845	−0.827	28.18	54.87	40.22	52.28	43.04	55.38	38.86
Fe I	4176.566	3.368	−0.805	12.43	36.47	20.32	25.93	25.63	31.03	23.19
Fe I	4181.755	2.831	−0.371	42.93	80.11	57.29	69.04	62.77	76.12	61.31
Fe I	4182.383	3.017	−1.180	6.88	28.61	16.67	18.49	17.39	24.40	15.01
Fe I	4184.891	2.831	−0.869	18.19	46.34	31.31	40.77	35.51	45.86	33.15
Fe I	4187.039	2.449	−0.548	62.34	81.58	66.77	85.12	69.22	89.05	71.25
Fe I	4187.795	2.425	−0.554	67.04	91.71	70.51	89.85	74.55	93.16	76.14
Fe I	4191.430	2.469	−0.666	55.47	75.82	63.40	82.67	65.01	85.41	63.29
Fe I	4195.329	3.332	−0.492	19.55	56.67	34.74	44.07	36.00	48.54	38.47
Fe I	4199.095	3.047	0.155	52.25	83.34	64.78	81.07	65.87	85.00	69.21
Fe I	4202.029	1.485	−0.708	——	——	98.63	——	——	——	——
Fe I	4213.647	2.845	−1.290	5.85	27.94	——	22.84	——	26.79	17.86
Fe I	4222.213	2.449	−0.967	42.42	70.07	51.65	67.29	55.23	70.27	54.11
Fe I	4233.602	2.482	−0.604	58.40	80.63	64.47	78.95	67.24	86.66	68.23
Fe I	4238.810	3.396	−0.233	19.49	52.32	36.40	41.37	41.81	43.91	35.08
Fe I	4250.119	2.469	−0.405	67.91	90.42	71.71	91.67	72.36	95.17	76.36
Fe I	4260.474	2.399	0.109	94.66	——	92.46	——	99.34	——	96.87
Fe I	4271.153	2.449	−0.349	76.56	——	87.23	——	96.48	——	92.10
Fe I	4282.403	2.176	−0.779	67.72	——	71.45	——	72.65	95.81	72.35
Fe I	4337.046	1.557	−1.695	66.34	——	60.76	85.76	68.69	89.26	63.66
Fe I	4430.614	2.223	−1.659	25.46	50.13	32.50	50.76	35.92	54.03	37.02
Fe I	4442.339	2.198	−1.255	46.21	79.59	53.66	75.54	58.65	80.42	58.74
Fe I	4443.194	2.858	−1.043	13.31	42.59	25.33	33.85	24.61	41.05	27.13
Fe I	4447.717	2.223	−1.342	37.50	69.72	48.78	68.01	49.06	71.68	50.40
Fe I	4459.117	2.176	−1.279	54.47	86.27	61.68	83.70	64.49	94.11	65.92
Fe I	4466.551	2.831	−0.600	52.03	74.98	54.73	77.26	56.46	85.01	57.88
Fe I	4494.563	2.198	−1.136	54.83	73.91	58.48	77.78	62.39	80.25	62.02
Fe II	4128.748	2.583	−3.578	——	10.39	——	——	——	9.14	6.15
Fe II	4178.862	2.583	−2.535	30.02	48.20	32.91	49.99	33.93	55.36	38.71
Fe II	4233.172	2.583	−1.947	64.62	——	55.78	87.66	56.99	——	63.87
Fe II	4416.830	2.778	−2.602	20.96	42.76	24.58	41.41	21.27	46.15	29.42
Fe II	4491.405	2.856	−2.756	12.83	29.31	14.43	25.39	18.70	32.05	17.97
Fe II	4508.288	2.856	−2.349	26.62	46.33	27.16	47.68	31.21	53.09	31.91
Fe II	4515.339	2.844	−2.540	21.71	37.70	22.43	38.41	24.73	——	25.50

Table A.2. List of lines used in the present analysis, with the individual abundances.

Species	λ(Å)	χ_{ex}(eV)	log gf	A(X) CS 30315-029	A(X) HE 0057-4541	A(X) HE 0105-6141	A(X) HE 0240-0807	A(X) HE 0516-3820	A(X) HE 0524-2055	A(X) HE 2229-4153
Mg I	3829.355	2.709	−0.231	4.75	5.60	5.40	5.15	5.65	5.65	5.55
Mg I	3832.304	2.710	0.146	4.65	5.70	5.45	5.30	5.50	5.65	5.50
Mg I	3838.290	2.720	0.415	4.85	5.65	5.40	5.25	5.50	5.50	5.60
Al I	3961.520	0.014	−0.323	2.68	3.50	3.20	3.26	3.30	3.40	3.25
Si I	4102.936	1.909	−2.827	4.80	5.94	5.64	5.30	5.45	5.37	5.48
S I	9212.860	6.525	0.420	—	5.40	5.25	4.95	—	5.05	5.10
S I	9228.090	6.525	0.260	4.25	5.25	—	—	—	5.10	—
S I	9237.540	6.525	0.040	4.40	5.40	—	—	5.35	—	5.00
K I	7664.911	0.000	0.130	2.63	—	—	3.00	3.18	—	3.30
K I	7698.974	0.000	−0.170	2.60	3.30	2.92	2.90	—	3.27	3.20
Ca I	4226.728	0.000	0.265	3.25	4.35	4.20	3.75	4.20	3.95	4.10
Ca I	4283.011	1.886	−0.292	3.40	4.60	4.35	3.98	4.40	4.22	4.40
Ca I	4289.367	1.879	−0.388	3.40	4.40	4.26	4.00	4.35	4.08	4.25
Ca I	4302.528	1.899	0.183	—	—	4.10	3.78	—	—	—
Ca I	4318.652	1.899	−0.295	3.40	4.36	4.20	3.85	4.32	4.05	4.22
Ca I	4425.437	1.879	−0.286	3.28	4.28	4.10	3.78	4.20	3.93	4.07
Ca I	4434.957	1.886	0.066	—	4.25	4.15	—	4.20	—	4.07
Ca I	4435.679	1.886	−0.412	—	4.25	4.12	—	—	—	4.02
Ca I	4454.779	1.899	0.335	3.22	4.25	4.08	3.70	4.12	3.86	4.03
Ca I	4455.887	1.899	−0.414	3.30	4.25	4.10	3.75	4.05	3.94	4.05
Sc II	3833.071	0.000	−2.014	−0.35	—	—	—	—	—	—
Sc II	4246.822	0.315	0.242	−0.40	0.80	0.80	0.38	0.74	0.40	0.62
Sc II	4294.767	0.605	−1.391	−0.25	0.92	0.85	—	—	0.52	—
Sc II	4314.083	0.618	−0.096	−0.39	0.84	0.78	0.42	0.72	0.35	0.64
Sc II	4320.732	0.605	−0.252	−0.42	0.82	0.73	0.38	0.75	0.40	0.61
Sc II	4354.598	0.605	−1.579	−0.28	—	—	—	—	—	—
Sc II	4374.457	0.618	−0.418	−0.42	0.80	0.77	0.36	0.76	0.42	0.62
Sc II	4400.389	0.605	−0.536	−0.40	0.82	0.72	0.36	0.74	0.43	0.60
Sc II	4415.557	0.595	−0.668	−0.36	0.87	0.76	0.40	0.77	0.45	0.62
V I	3855.841	0.069	0.013	—	1.70	—	—	—	—	—
V I	4111.774	0.301	0.408	—	1.50	1.35	1.05	—	—	1.35
V I	4379.230	0.301	0.580	0.32	1.60	1.38	1.18	1.40	1.22	1.34
V I	4384.712	0.287	0.510	—	1.48	1.24	—	—	—	1.30
V I	4389.976	0.275	0.200	—	—	—	—	—	—	—
V I	4408.193	0.275	0.020	—	—	—	—	—	—	1.42
V II	3715.466	1.575	−0.250	0.50	1.88	1.68	1.28	1.58	1.27	1.50
V II	3727.343	1.687	−0.231	—	1.78	1.70	1.30	1.70	1.33	1.46
V II	3732.750	1.565	−0.354	0.55	1.87	1.64	1.30	1.68	1.32	1.58
V II	3750.870	1.679	−0.409	—	—	—	1.32	—	1.25	1.38
V II	3899.129	1.805	−0.784	—	1.92	—	—	—	—	—
V II	3916.411	1.428	−1.053	—	1.90	1.72	1.40	1.75	1.38	1.52
V II	3951.960	1.476	−0.784	0.45	1.80	1.60	1.26	1.60	1.30	1.45
V II	4002.936	1.428	−1.447	—	1.90	—	1.38	—	1.40	1.57
V II	4005.705	1.817	−0.522	0.62	1.90	1.65	1.45	—	1.37	1.60
V II	4023.378	1.805	−0.689	—	1.86	1.55	1.50	1.80	1.40	—
V II	4035.622	1.793	−0.767	—	—	—	1.47	—	—	—
Cr I	4254.332	0.000	−0.114	1.78	3.05	2.90	2.22	3.05	2.35	2.75
Cr I	4274.796	0.000	−0.231	1.77	3.10	2.78	2.35	3.05	2.50	2.78
Cr I	4289.716	0.000	−0.361	1.80	3.04	2.80	2.32	3.05	2.46	2.73
Mn I	4030.753	0.000	−0.470	1.15	2.40	2.00	1.67	2.28	1.80	2.10
Mn I	4033.062	0.000	−0.618	1.17	2.35	2.00	1.60	2.25	1.83	2.15
Mn I	4034.483	0.000	−0.811	1.25	2.50	2.20	1.70	2.35	1.85	2.17
Mn I	4041.355	2.114	0.285	1.58	2.78	2.37	2.07	2.73	2.30	2.42
Mn I	4082.939	2.178	−0.354	—	—	—	—	—	2.22	—
Co I	3845.461	0.923	0.010	1.62	2.72	2.85	2.20	2.70	2.30	2.50
Co I	3995.302	0.923	−0.220	1.66	2.71	2.68	2.18	2.74	2.28	2.55
Co I	4118.767	1.049	−0.490	1.80	2.95	2.70	2.35	2.76	2.60	2.65
Co I	4121.311	0.923	−0.320	1.88	3.05	2.95	2.42	3.05	2.60	2.82
Ni I	3807.138	0.423	−1.205	2.85	3.80	3.95	3.36	3.85	3.40	3.70
Ni I	3858.292	0.423	−0.936	2.70	3.78	3.55	3.25	3.85	3.38	3.70
Sr II	4077.719	0.000	0.170	−0.82	0.82	0.60	−0.10	0.63	0.15	0.53
Sr II	4215.519	0.000	−0.170	−0.86	0.77	0.68	−0.06	0.66	0.14	0.60
Y II	3774.331	0.130	0.210	−1.47	−0.37	−0.30	−0.72	—	−0.82	−0.50
Y II	3788.694	0.104	−0.070	−1.48	−0.26	−0.50	−0.76	−0.13	−0.74	−0.54
Y II	3818.341	0.130	−0.980	−1.44	—	—	−0.69	—	−0.62	−0.40
Y II	3950.352	0.104	−0.490	−1.43	−0.26	−0.38	−0.74	−0.14	−0.69	−0.40
Y II	4398.013	0.130	−1.000	−1.43	—	—	−0.70	—	−0.68	−0.53
Zr II	3836.762	0.559	−0.060	−0.87	0.51	0.12	−0.22	0.55	−0.03	0.15
Zr II	4161.213	0.713	−0.720	−0.67	0.60	—	0.15	0.64	0.25	0.33
Zr II	4208.977	0.713	−0.460	−0.76	0.51	0.30	−0.02	0.35	0.03	0.18
Zr II	4317.299	0.713	−1.380	—	0.52	—	—	—	0.20	—
Mo I	3864.103	0.000	−0.010	< −1.15	—	—	—	—	< −0.35	—
Ru I	3498.942	0.000	0.310	−0.90	—	—	< −0.20	—	< −0.40	—
Ru I	3728.025	0.000	0.270	−1.00	0.24	—	< −0.20	<0.10	−0.25	< −0.15
Ru I	3799.349	0.000	0.020	< −0.60	<0.20	—	< −0.20	—	−0.05	< −0.10
Pd I	3404.579	0.814	0.320	< −1.00	—	—	—	—	—	< −0.60
Pd I	3516.944	0.962	−0.240	< −1.20	—	—	—	—	—	—
Ba II	4554.020	0.000	0.170	−1.10	−0.22	−0.25	−0.50	−0.27	−0.63	−0.65
La II	3759.080	0.244	−0.030	−2.05	−1.20	—	−1.55	—	−1.58	−1.65
La II	3794.770	0.244	0.210	−1.92	−1.04	−1.25	−1.40	−1.20	−1.60	−1.50
La II	3849.010	0.000	−0.973	−2.15	−0.95	—	−1.40	—	−1.55	−1.65
La II	3929.210	0.173	−0.320	−2.00	−0.90	—	−1.46	—	−1.60	—
La II	3949.100	0.403	0.490	−2.10	−0.98	−1.25	−1.50	—	−1.55	−1.50
La II	3988.507	0.403	−0.969	−2.15	−1.03	−1.13	−1.40	—	−1.60	−1.60
La II	3995.750	0.173	−1.084	−2.03	−0.93	−1.03	−1.50	—	−1.57	−1.62
La II	4077.340	0.235	−0.060	−2.07	−1.03	—	−1.40	—	−1.58	—

Table A.2. continued.

Species	λ(Å)	χ_{ex}(eV)	loggf	A(X) CS 30315-029	A(X) HE 0057-4541	A(X) HE 0105-6141	A(X) HE 0240-0807	A(X) HE 0516-3820	A(X) HE 0524-2055	A(X) HE 2229-4153
La II	4086.708	0.000	−0.696	−2.01	−1.03	—	−1.48	—	−1.57	−1.60
La II	4123.221	0.321	−0.850	−2.14	−1.07	−1.08	−1.51	−1.16	−1.54	−1.50
La II	4196.550	0.321	−0.300	−2.10	−0.98	—	−1.40	—	−1.60	—
La II	4238.370	0.403	−0.260	−2.04	—	—	—	—	—	—
La II	4333.753	0.173	−0.060	−2.04	—	—	−1.35	—	−1.56	—
La II	4429.910	0.235	−0.350	−2.10	−1.08	—	−1.35	—	−1.54	—
Ce II	3942.151	0.000	−0.180	−1.60	< −0.42	—	< −0.92	—	−1.30	< −1.00
Ce II	3999.237	0.090	0.060	−1.95	< −0.68	—	−1.20	—	−1.40	—
Ce II	4053.503	0.000	−0.610	−1.60	< −0.40	—	< −0.90	—	—	—
Ce II	4073.474	0.478	0.230	−1.75	−0.56	—	−1.00	< −0.40	−1.20	—
Ce II	4083.222	0.701	0.270	−1.70	—	—	< −0.80	—	—	—
Ce II	4120.827	0.320	−0.210	−1.55	< −0.20	—	−0.90	—	< −1.00	—
Ce II	4127.364	0.684	0.350	−1.70	< −0.54	< −0.85	−0.98	—	< −1.20	< −1.00
Ce II	4137.645	0.516	0.400	−1.62	−0.52	—	—	—	−1.20	−1.10
Ce II	4142.397	0.696	0.220	−1.60	—	—	—	—	—	—
Ce II	4144.996	0.696	0.100	−1.60	−0.35	—	—	—	—	—
Ce II	4222.597	0.122	0.020	−1.65	−0.50	—	−1.02	−0.44	−1.15	−1.00
Ce II	4382.165	0.684	0.130	−1.60	< −0.40	—	< −0.88	—	< −1.10	—
Ce II	4418.780	0.864	0.280	−1.45	—	—	—	—	−1.16	—
Ce II	4449.330	0.609	0.040	−1.90	—	—	−1.00	< −0.30	—	—
Ce II	4486.909	0.295	−0.260	−1.55	< −0.54	—	−0.90	< −0.30	−1.16	—
Pr II	3964.820	0.055	0.069	< −2.20	—	—	< −1.60	—	—	—
Pr II	3965.260	0.204	0.204	< −2.10	—	—	< −1.60	—	—	—
Pr II	4038.455	0.000	−0.510	−2.10	—	—	—	—	—	—
Pr II	4044.813	0.000	−0.293	−2.15	< −1.00	< −0.70	−1.50	—	< −1.50	—
Pr II	4096.820	0.216	−0.255	< −1.90	—	—	< −1.60	—	< −1.60	—
Pr II	4143.120	0.371	0.604	−2.08	< −1.15	< −0.84	—	—	−1.70	< −1.40
Pr II	4179.400	0.204	0.459	−2.16	—	—	−1.42	< −0.75	−1.45	—
Pr II	4222.950	0.055	0.235	< −2.14	—	—	−1.54	—	—	—
Pr II	4408.820	0.000	0.053	−2.15	< −1.12	< −1.00	−1.60	< −1.00	−1.70	-1.50
Pr II	4496.470	0.216	−0.762	< −2.20	—	—	—	—	—	—
Pr II	4510.150	0.422	−0.007	< −1.85	—	—	—	—	—	—
Nd II	4012.700	0.000	−0.600	−1.55	< −0.50	< −0.38	< −1.00	< −0.20	—	—
Nd II	4018.833	0.064	−0.850	< −1.50	—	—	—	—	—	—
Nd II	4021.327	0.321	−0.100	−1.60	−0.60	—	−1.10	—	−1.16	—
Nd II	4059.950	0.204	−0.520	−1.60	—	< −0.25	—	—	—	—
Nd II	4061.080	0.471	0.550	−1.62	−0.50	−0.50	−0.92	−0.54	−1.10	−1.02
Nd II	4069.265	0.064	−0.570	−1.50	—	—	−0.78	—	−0.95	—
Nd II	4109.448	0.321	0.350	−1.50	−0.53	−0.58	−0.88	−0.47	−1.04	−0.97
Nd II	4232.374	0.064	−0.470	−1.60	−0.58	—	−1.00	—	−1.05	—
Nd II	4358.160	0.320	−0.160	—	—	−0.52	—	—	−1.05	—
Nd II	4368.630	0.064	−0.810	−1.60	—	—	−0.90	—	−0.98	—
Nd II	4385.660	0.204	−0.300	−1.60	—	—	−0.95	—	−1.04	—
Nd II	4400.820	0.064	−0.600	−1.48	—	—	−0.92	—	−0.94	—
Nd II	4446.384	0.205	−0.350	−1.55	−0.60	—	−0.90	−0.45	−1.10	—
Nd II	4451.500	0.205	−0.350	—	—	—	−0.90	−0.36	−1.00	—
Nd II	4501.810	0.204	−0.690	−1.50	—	—	< −0.80	—	−0.95	—
Sm II	3793.978	0.104	−0.498	< −2.00	—	—	—	—	—	—
Sm II	3896.972	0.041	−0.578	< −1.80	—	—	—	—	< −1.48	—
Sm II	4023.222	0.041	−0.830	< −1.73	—	—	—	—	—	—
Sm II	4068.324	0.434	−0.743	< −1.60	—	—	< −0.86	—	—	—
Sm II	4183.767	0.041	−0.999	−1.68	< −0.80	—	−1.20	—	< −1.30	—
Sm II	4256.391	0.378	−0.135	−1.75	−0.88	—	—	—	−1.30	< −1.20
Sm II	4318.927	0.277	−0.268	−1.72	−1.05	−0.80	−1.18	< −0.46	−1.40	−1.25
Sm II	4421.126	0.378	−0.477	−1.70	—	—	< −1.15	—	—	—
Sm II	4467.341	0.659	0.303	−1.95	< −0.90	—	−1.32	—	−1.55	−1.40
Sm II	4499.475	0.248	−1.000	< −1.60	—	—	−1.04	—	—	—
Eu II	3724.931	0.000	−0.090	−2.32	−1.23	—	−1.56	< −1.10	−1.75	< −1.70
Eu II	3930.499	0.207	0.270	−2.18	−1.30	−1.60	−1.62	−1.35	—	−1.72
Eu II	3971.972	0.207	0.270	−2.30	−1.30	—	−1.65	—	—	−1.70
Eu II	4129.725	0.000	0.220	−2.20	−1.25	−1.55	−1.53	−1.37	−1.75	−1.74
Eu II	4205.042	0.000	0.210	−2.22	−1.25	−1.45	−1.52	−1.30	−1.74	−1.72
Gd II	3768.396	0.360	0.210	−1.90	−0.90	< −1.00	−1.25	−1.12	−1.40	−1.40
Gd II	3796.384	0.032	0.140	—	−0.80	< −0.80	−1.12	—	−1.40	−1.25
Gd II	3836.915	0.492	−0.322	—	—	—	< −1.12	—	—	—
Gd II	3844.578	0.144	−0.400	−1.80	< −0.65	—	−0.90	—	−1.35	< −1.10
Gd II	4085.558	0.731	0.070	—	—	—	−1.10	—	< −1.35	—
Gd II	4130.366	0.731	0.160	< −1.75	—	—	< −1.10	—	< −1.40	—
Gd II	4191.075	0.427	−0.570	—	—	—	—	—	< −1.10	—
Tb II	3702.845	0.126	−0.147	< −2.40	—	—	< −1.75	—	< −1.90	—
Tb II	3874.180	0.000	−0.317	< −2.60	—	—	< −1.80	—	< −2.00	—
Tb II	4005.467	0.126	−0.020	−2.40	—	—	—	—	—	—
Dy II	3694.810	0.103	−0.110	< −1.70	−0.60	—	−1.03	—	−1.17	−1.32
Dy II	3757.368	0.103	−0.170	−1.65	—	—	−0.96	< −0.45	−1.14	—
Dy II	3788.436	0.103	−0.570	−1.72	—	—	−1.15	< −0.10	−1.11	—
Dy II	3869.864	0.000	−1.050	−1.65	—	—	—	—	—	—
Dy II	3944.681	0.000	0.100	−1.60	−0.62	−0.98	−1.05	−0.70	−1.16	−1.18
Dy II	3996.689	0.590	−0.200	−1.74	—	—	−1.02	—	—	—
Dy II	4077.966	0.103	0.210	−1.60	−0.65	< −0.90	−0.99	−0.75	−1.13	−1.16
Dy II	4103.306	0.103	−0.390	−1.48	< −0.50	—	−0.98	< −0.30	−1.10	−1.20
Dy II	4111.343	0.000	−0.850	−1.52	< −0.45	—	−1.06	—	−1.05	−0.90
Ho II	3796.745	0.000	−0.745	−2.35	−1.32	—	−1.60	< −1.00	−1.80	−1.90
Ho II	3810.734	0.000	−0.678	−2.40	—	—	−1.65	—	—	—
Er II	3692.649	0.055	0.138	−1.80	−0.80	—	−1.25	< −0.78	−1.30	−1.24
Er II	3786.836	0.000	−0.644	−1.60	< −0.60	—	−1.15	—	−1.18	−1.10
Er II	3830.482	0.000	−0.365	−1.85	−0.75	—	−1.26	—	−1.30	< −1.20
Er II	3896.234	0.055	−0.241	—	—	—	−1.23	—	—	—

Table A.2. continued.

Species	λ(Å)	χ_{ex}(eV)	loggf	A(X) CS 30315-029	A(X) HE 0057-4541	A(X) HE 0105-6141	A(X) HE 0240-0807	A(X) HE 0516-3820	A(X) HE 0524-2055	A(X) HE 2229-4153
Er II	3938.626	0.000	−0.520	< −1.82	< −0.70	—	−1.22	—	−1.30	—
Tm II	3701.363	0.000	−0.540	< −2.40	—	—	—	—	—	—
Tm II	3795.760	0.029	−0.230	−2.65	< −1.46	—	< −1.78	—	—	< −1.95
Tm II	3848.020	0.000	−0.130	−2.78	< −1.45	—	< −1.94	—	—	< −1.90
Yb II	3694.199	0.000	−0.300	−1.98	−0.95	−1.22	−1.25	−0.97	−1.58	−1.53
Os I	4260.849	0.000	−1.470	< −1.00	—	—	< −0.40	—	—	—
Os I	4420.468	0.000	−1.530	—	—	—	< −0.45	—	—	—
Ir I	3513.648	0.000	−1.260	< −0.74	<0.12	—	< −0.20	—	< −0.45	—
Ir I	3800.120	0.000	−1.450	—	< −0.10	—	—	—	—	—
Th II	4019.129	0.000	−0.228	−2.45	< −1.40	—	< −1.92	—	< −2.12	—